JBC RESEARCH ARTICLE

Structural and functional analysis of *Pseudomonas aeruginosa* PelA provides insight into the modification of the Pel exopolysaccharide

Received for publication, February 6, 2025, and in revised form, March 14, 2025 Published, Papers in Press, March 20, 2025,
https://doi.org/10.1016/j.jbc.2025.108432

Jaime C. Van Loon[1,2], François Le Mauff[3,4,5,6], Mario A. Vargas[1], Stephanie Gilbert[1], Roland Pfoh[1], Zachary A. Morrison[7], Erum Razvi[1,2], Mark Nitz[7], Donald C. Sheppard[3,4,5], and P. Lynne Howell[1,2,*]

From the [1]Program in Molecular Medicine, The Hospital for Sick Children, Toronto, Ontario, Canada; [2]Department of Biochemistry, University of Toronto, Toronto, Ontario, Canada; [3]Department of Microbiology and Immunology, Faculty of Medicine, McGill University, Montreal, Quebec, Canada; [4]Infectious Disease and Immunity in Global Health, Research Institute of the McGill University Health Centre, Montreal, Quebec, Canada; [5]McGill Interdisciplinary Initiative in Infection and Immunity, Montreal, Quebec, Canada; [6]GlycoNET Integrated Services, Microbial Glycomic Node, Montreal, Quebec, Canada; [7]Department of Chemistry, University of Toronto, Toronto, Ontario, Canada

Reviewed by members of the JBC Editorial Board. Edited by Chris Whitfield

A major biofilm matrix determinant of *Pseudomonas aeruginosa* is the partially deacetylated α-1,4 linked *N*-acetylgalactosamine polymer, Pel. After synthesis and transport of the GalNAc polysaccharide across the inner membrane, PelA partially deacetylates and hydrolyzes Pel before its export out of the cell *via* PelB. While the Pel modification and export proteins are known to interact in the periplasm, it is unclear how the interaction of PelA and PelB coordinates these processes. To determine how PelA modifies the polymer, we determined its structure to 2.1 Å and found a unique arrangement of four distinct domains. We have shown previously that the hydrolase domain exhibits endo-α-1,4-*N*-acetylgalactosaminidase activity. Characterization of the deacetylase domain revealed that PelA is the founding member of a new carbohydrate esterase family, CE21. Further, we found that the PelAB interaction enhances the deacetylation of *N*-acetylgalactosamine oligosaccharides. Using the PelA structure in conjunction with AlphaFold2 modeling of the PelAB complex, we propose a model wherein PelB guides Pel to the deacetylase domain of PelA and subsequently to the porin domain of PelB for export. Perturbation or loss of the PelAB interaction would result in less efficient deacetylation and potentially increased Pel hydrolysis. In PelA homologs across many phyla, the predicted structure and active sites are conserved, suggesting a common modification mechanism in Gram-negative bacterial species containing a functional *pel* operon.

Biofilms are communities of microbial cells surrounded by an extracellular matrix composed of polysaccharides, proteins, surfactants, lipids, extracellular DNA, and other nucleic acids (1, 2). The extracellular matrix is an important virulence factor that enables the embedded microbes to evade the host immune system and affects the efficacy of some antibiotics (3). The Gram-negative bacterium *Pseudomonas aeruginosa* predominantly exists as a biofilm and is commonly found in chronic infections, such as in the lungs of individuals with cystic fibrosis or burn wounds (4, 5). *P. aeruginosa* has the genetic capacity to produce three different exopolysaccharides, each important for biofilm formation: alginate, Psl, and Pel (6). Pel provides structural support by forming interactions with extracellular DNA in the biofilm matrix (7), aids in maintaining cell-to-cell interactions (8), interacts with abundant anionic host polymers in the sputum of individuals with cystic fibrosis (9), protects cells against aminoglycoside antibiotics (8, 10), helps the biofilm-embedded cells remain associated with the surface under starvation conditions (11), and provides a competitive advantage in pellicle biofilms under oxygen-limited conditions (12).

Pel is an α-1,4–linked linear polysaccharide that exists in both cell-associated and cell-free (also referred to as matrix-associated) forms (13). While the structure of the cell-associated form has yet to be determined, the cell-free form of Pel is composed predominantly of dimeric repeats of galactosamine (GalN) and GalNAc (14). The biosynthesis of Pel in *P. aeruginosa* occurs *via* a synthase-dependent pathway and requires the proteins encoded by the *pelABCDEFG* operon (15, 16). In the cytoplasm, the PelDEFG complex synthesizes and transports the growing polysaccharide across the inner membrane (17). Once in the periplasm, the large 948-residue protein PelA modifies Pel using its two enzymatic domains. PelA's deacetylase domain selectively removes acetyl groups from the polysaccharide, rendering Pel cationic (18), while its glycoside hydrolase (GH) family 166 (GH166) domain hydrolyzes Pel. The hydrolase activity is required for the generation of the cell-free form of the polysaccharide, which is important for the biomechanical properties of the biofilm and *P. aeruginosa* virulence (13, 19). PelB is a large protein proposed to help guide mature Pel through the periplasm using its tetratricopeptide repeats (TPRs). The β-barrel domain of PelB

* For correspondence: P. Lynne Howell, howell@sickkids.ca.

exports Pel to the extracellular space with the aid of the oligomeric lipoprotein PelC (20, 21).

Interactions between modification enzymes and the periplasmic TPRs of outer membrane porin proteins are a common feature of synthase-dependent exopolysaccharide biosynthetic pathways with the modification and export of poly-β(1,6)-*N*-acetylglucosamine (PNAG) and *P. aeruginosa* alginate being coupled through the PgaB–PgaA and AlgX–AlgK–AlgE interactions, respectively (22–26). We have previously demonstrated that the modification and export of *P. aeruginosa* Pel is dependent on PelA interacting with six of the TPR repeats of PelB—TPR9-TPR14—and that this interaction results in an increase and decrease in PelA's deacetylase and hydrolase activities, respectively (21). However, how the multidomain, dual-active protein PelA binds to and modifies Pel and the interaction with PelB modulates its activities prior to export of Pel for use in the *P. aeruginosa* biofilm is currently unknown.

Herein, we present the crystal structure of PelA from *Pseudomonas thermotolerans* (*Pt*PelA) and show that the protein has a unique four-domain structure. Using pseudo-substrates and α-1,4-GalNAc oligosaccharides, we demonstrate that *Pt*PelA and its ortholog *P. aeruginosa* PelA (*Pa*PelA) exhibit hydrolase and deacetylase activity and that the deacetylase activity is enhanced when *Pa*PelA is incubated with its interaction partner, *P. aeruginosa* PelB (*Pa*PelB). In conjunction with Alphafold2 (AF2) modeling, we propose a model wherein *Pa*PelB guides Pel to the deacetylase domain of *Pa*PelA prior to export for use in the *P. aeruginosa* biofilm. If the interaction with *Pa*PelB is perturbed or lost, we hypothesize that *Pa*PelA can then hydrolyze the polysaccharide. The high degree of structural conservation of PelA across Gram-negative species suggests that the hydrolase and deacetylase activities of its homologs are essential for bacterial species that contain a functional *pel* operon.

Results

PelA has a compact four-domain structure

To gain insight into the structure and function of PelA, we undertook structural studies of *Pa*PelA and a thermotolerant ortholog from *P. thermotolerans* (72% amino acid sequence identity and 83% similarity to *Pa*PelA). While *Pa*PelA did not readily crystalize, a construct of *Pt*PelA excluding the predicted signal sequence, encompassing residues 37 to 937, crystallized in various conditions. Diffraction data were collected for selenomethionyl-incorporated (SeMet) *Pt*PelA at the National Synchrotron Light Source-II to 2.1 Å, and the structure was solved using the single-wavelength anomalous diffraction method (27). Iterative refinement resulted in a R_{work} and R_{free} of 18.17% and 22.64%, respectively (Table 1). Structural analysis of *Pt*PelA reveals four distinct domains (Fig. 1, *A* and *B*) that align well with the AF2 model of *Pa*PelA (*Pa*PelA^{AF2}; Figure . S1; 1.6 Å RMSD over 816 α-carbons) (28). As the quality of the electron density prevented us from building residues 83 to 105, 198, 321 to 323, 389 to 395, 417 to 420, 448, 588 to 614, and 703 to 718 in the *Pt*PelA structure, both the *Pt*PelA and *Pa*PelA^{AF2} models were used during our structural analyses.

Table 1
X-ray data collection and refinement statistics

	*Pt*PelA$^{37\text{-}937}$ SeMet
Data collection	
Wavelength (Å)	0.979338
Temperature (K)	100
Space group	$P2_12_12_1$
Cell dimensions	
a, *b*, *c* (Å)	80.6, 93.6, 124.1
α, *β*, *γ* (°)	90, 90, 90
Resolution (Å)	29.45–2.09 (2.17–2.09)[a]
Total no. of reflections	107,132 (10,527)
No. of unique reflections	56,194 (5481)
R_{merge} (%)[b]	12.50 (54.70)
Average I/σ (I)	15.04 (3.45)
Completeness (%)	99.50 (96.90)
Redundancy (%)	13.75 (13.45)
Refinement	
Resolution (Å)	29.45–2.09 (2.17–2.09)[a]
R_{work}/R_{free} (%)[c]	18.17/22.64
No. of atoms	
Protein	6359
Ligand/ion	0
Water	428
B-factors	
Protein	33.30
Ligand/ion	
Water	33.02
R.m.s.ds	
Bond lengths (Å)	0.011
Bond angles (°)	1.090
Ramachandran plot[d]	
Total favored (%)	96.89
Total allowed (%)	2.98
PDB	9CGY

[a] The values in parentheses correspond to the highest resolution shell.
[b] $R_{merge} = \sum\sum|I(k) - \langle I\rangle|/\sum I(k)$, where $I(k)$ and $\langle I\rangle$ represent the diffraction intensity values of the individual measurements and the corresponding mean values, respectively. The summation is over all unique measurements.
[c] $R_{work} = \sum||F_{obs}| - k|F_{calc}||/|F_{obs}|$, where F_{obs} and F_{calc} are the observed and calculated structure factors, respectively. R_{free} is the sum extended over a subset of reflections (10%) excluded from all stages of the refinement.
[d] As calculated using MOLPROBITY.

The N-terminal hydrolase domain, residues 37 to 292, has a β_{12}/α_9-barrel-fold that aligns closely to the structure of the isolated *Pa*PelA hydrolase domain (*Pa*PelA$_H$, PDB 5TCB; 0.6 Å RMSD over 224 α-carbons) (Fig. 1*C*) (19). The hydrolase domains of *Pt*PelA and *Pa*PelA$_H$ have a deep binding groove (Fig. 1*B*), which we have previously shown hydrolyzes GalNAc polymers but which can also tolerate the presence of some GalN (14, 19).

Previous bioinformatics analyses have suggested that residues 303 to 409 in *Pa*PelA and residues 293 to 398 in *Pt*PelA are structurally similar to reductase enzymes (18). Upon analysis of the *Pt*PelA structure, we found that residues 293 to 498 form a mixed α/β domain with 12 β-strands (Fig. 1, *B* and *D*). Six β-strands (β2-β1-β3-β4-β10-β9b) run roughly parallel to each other through the center of the domain surrounded by five α-helices. In *Pa*PelA, the ninth β-strand forms the central strand of a five stranded β-sheet (β5-β7-β9a-β8-β6). In contrast, in the *Pt*PelA crystal structure, there is a discontinuity in β9 (Fig. 1*D*). While β9b is situated with β1-4 and β10, β9a is grouped with β5-8. There is a pair of β-strands (β11–12) that are surface exposed and physically adjacent to the deacetylase domain and an additional β-strand (denoted β15) that comes after the α6 helix, which contributes to the

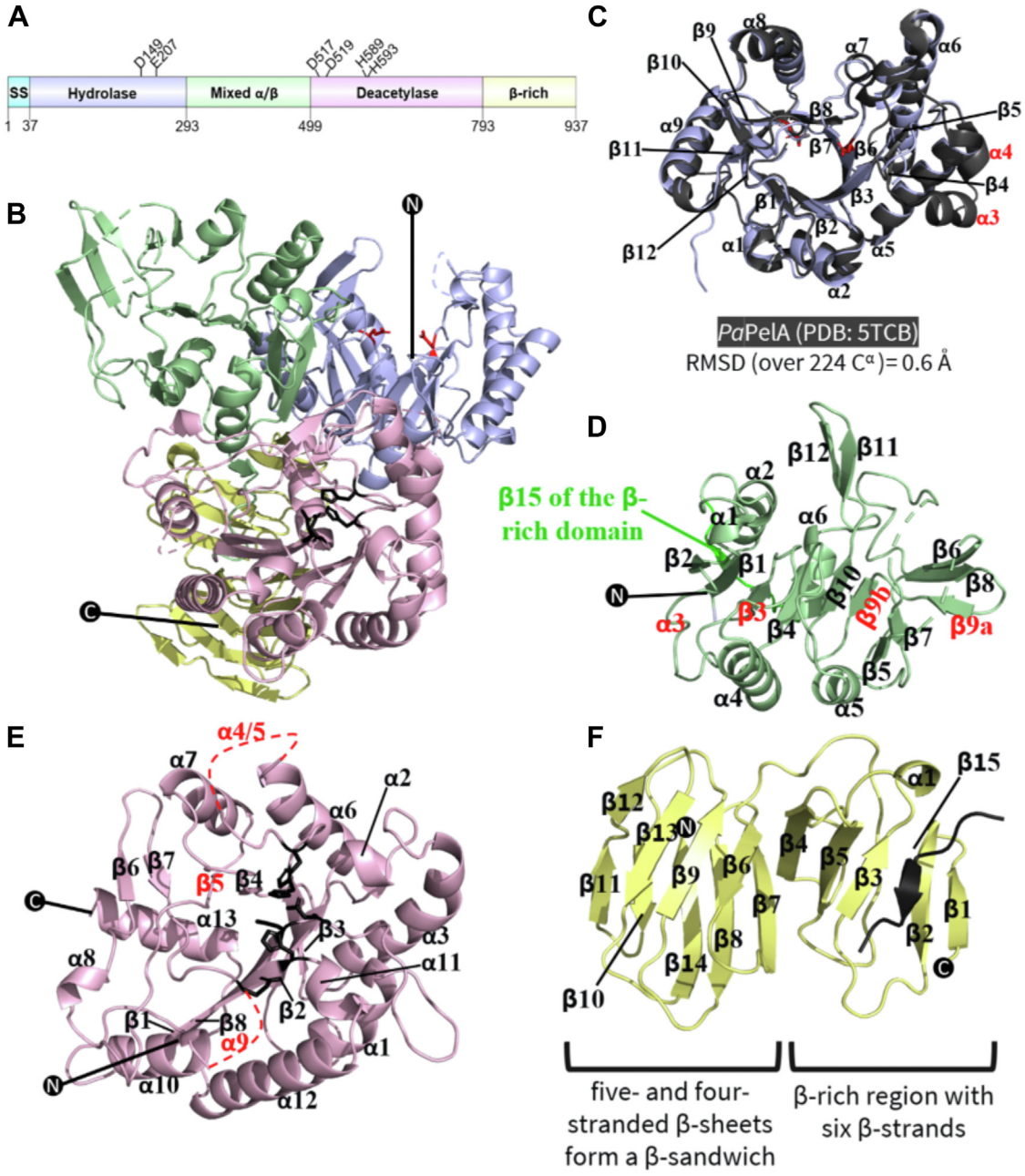

Figure 1. The full-length structure of *Pt*PelA. *A*, linear representation of *Pt*PelA domains based on the structure and available literature. The domain architecture was visualized using DOG 2.0 Illustrator of Protein Domain Structures (77). Amino acids that are required for enzymatic activity are highlighted. *B*, cartoon representation of the crystal structure of residues 37 to 937 of *Pt*PelA shown in two opposing views. The domains as colored as depicted in (*A*). Amino acids required for the deacetylase and hydrolase activities are shown in *black* and *red*, respectively. N and C represent the N- and C-termini, respectively. The dashed lines represent regions of the protein that could not be built due to the poor quality of the electron density. *C*, comparison of the hydrolase domain of PelA as determined from the structure from *Pseudomonas thermotolerans* (*blue*) and the structure of *Pa*PelA$_H$ (5TCB, *gray*) with the secondary structure labeled. Secondary structural elements in the AF2 model of *Pa*PelA that are missing in the structure of *Pt*PelA are labeled in *red*. *D*, the mixed α/β domain of *Pt*PelA. *E*, the deacetylase domain of *Pt*PelA. *F*, the β-rich domain of *Pt*PelA. SS, signal sequence.

structure of the β-rich domain (Fig. 1, *D* and *F*). To provide insight into the function of this protein, we compared the structure of the mixed α/β domain of *Pt*PelA to the other experimentally determined structures using the DALI server (29). The DALI hits identified have less than 15% sequence identity to *Pa*PelA and have several differences in their secondary structures (Fig. S2*A*). Examination of the function of the top DALI hits suggests that this domain of PelA could bind carbohydrate and/or be important for mediating the interaction between PelA and PelB, as ThuA-like proteins are involved in the utilization of trehalose (30), while the region of 2-amino-2-deoxyisochorismate synthase PhzE and the intraflagellar transport protein component IFT52 that aligns to *Pt*PelA binds chorismate (31) and helps bridge interactions between the IFT-B1 and B2 components of this intracellular transport complex, respectively (32).

The deacetylase domain of *Pa*PelA (residues 520–804) has previously been predicted to have structural similarity to CE4 enzymes (18, 33). Using DALI, amino acids 499 to 792 of *Pt*PelA reveal similarity to CE4 and CE18 enzymes (34, 35). The deacetylase domain of *Pa*PelA has the core $(\beta/\alpha)_7$-fold, which is characteristic of CE enzymes (Fig. 1*E*) (22, 34–37). There are also addition structural features including short α-helices between the second and seventh β/α pairs, a 31-amino acid loop containing two small α-helices between the third β/α pair and a short β-strand and α-helix between the sixth β/α pair. Lastly, there is an α-helix after the last β/α pair that extends towards the final domain of PelA (Fig. 1*E*). In our crystal structure, we were unable to model residues 588 to 614 and 703 to 719. Modeling of these residues by AF2 in *Pa*PelA^{AF2} suggests that these unstructured loops are important for forming a 23 Å-deep, 44 Å-long binding groove. The dimensions of this groove correspond to the length of a $(GalNAc)_9$ polymer (Fig. 2*A*) (38).

*Pt*PelA also contains a 14-stranded β-rich region comprised of two distinct regions (residues 793–937) (Fig. 1*F*). The first β-rich region has six β-strands (β1-5 and β15), with a short α-helix positioned between β3 and β4. As described above, strand β15 is contributed from the mixed α/β domain (Fig. 1*F*). The second β-rich region consists of five- and four-stranded β-sheets that together form a β-sandwich (β6-14). While DALI analyses reveals that the alginate lyase Dp0100 aligns to the entire β-rich domain of *Pt*PelA, the xylanase B GH and chitinase ChiD hits only align to the β-sandwich region of this domain (39–42) (Fig. S2*B*). The nine-stranded β-jelly domain of xylanase B has not been shown to bind xylan but is required for the function of GH family 30 enzymes (39, 40). Similarly, while the 16-stranded β-sandwich domain of Dp0100 has not been shown to bind alginate (41), the presence of a β-jelly domain in alginate lyases is a common occurrence. The eight-stranded β-jelly domain of ChiD not only provides structural rigidity but this domain is also predicted to help generate a long chitin-binding site (42). Combined, this suggests that the β-rich domain could provide structural stability to *Pt*PelA and facilitate carbohydrate binding.

PelA is structurally similar to CE4 and CE18 family members

PelA deacetylase activity is essential for *P. aeruginosa* biofilm formation as chromosomal point mutation of residues in the putative deacetylase active site results in no adherence in a biofilm assay (18). As PelA is not currently part of any CAZy carbohydrate esterase (CE) family, to gain insight into PelA's mechanism of action, we next used the DALI server to determine whether it is structurally similar to any previously characterized CEs. We found structural similarities to members of the CE4 and CE18 superfamilies and have used *Streptococcus pneumoniae* PgdA (*Sp*PgdA) and *Aspergillus fumigatus* Agd3, respectively, as representative members of these families (34, 35). As noted previously as we were unable to model residues 588 to 614 and 703 to 718 in *Pt*PelA, we have therefore used *Pa*PelA^{AF2} for our comparisons. We found that while *Pa*PelA^{AF2} aligns poorly to *Sp*PgdA and Agd3 with RMSDs of 4.6 and 5.0 Å over 184 α-carbons, respectively, six significant structural differences between *Pa*PelA^{AF2} and *Sp*PgdA/Agd3 could be defined (Fig. 3). The structural differences between *Pa*PelA^{AF2} and *Sp*PgdA contribute to a deeper and more elongated active site groove in *Pa*PelA^{AF2} relative to *Sp*PgdA (Fig. 3, *A* and *B*), while differences between *Pa*PelA and Agd3 similarly affect the orientation and length of active site groove (Fig. 3, *C* and *D*). The remaining differences between *Pa*PelA^{AF2} and *Sp*PgdA/Agd3 are in the active site.

CE4 and CE18 family members have five and four canonical active site motifs, MT1-5 and CM1-4, respectively (Fig. 2, *B* and *C*). Residues D528 and D530 of *Pa*PelA are a part of MT1/CM1, while residues H600 and H604 are located in MT2/CM2. D528 is the putative catalytic base, whereas D530, H600, and H604 are predicted to be essential for coordinating the divalent cation required for deacetylation. The arginine residue found in MT3/CM3, which is responsible for activating the catalytic base in CE4 and C18 enzymes, is not conserved in *Pa*PelA. Compared to CE4 enzymes, *Pa*PelA is missing the α-insertion preceding β6 that orients MT3 in the CE4 active site (Fig. 3, *A* and *B*, yellow). In Agd3, the conserved arginine is situated on the α-insertion after β6 loop (Fig. 3, *C* and *D*, blue) and while this insertion is present in *Pa*PelA, the loop is oriented differently, and there is no conserved arginine residue in *Pa*PelA's CM3. In contrast to CE4 and CE18 enzymes, *Pa*PelA contains a conserved histidine residue (H526), found in MT1, that aligns closely to the arginine residues in Agd3 and *Sp*PgdA (Fig. 2*B*). Finally, E723 in *Pa*PelA is a part of MT4, which is predicted to activate H761, the catalytic acid in MT5/CM4. The apparent lack of an activating arginine in the MT3/CM3 active site motif suggests that *Pa*PelA likely operates *via* a modestly different mechanism than the CE4 and CE18 enzymes and potentially utilizes H526 to activate the catalytic base.

PtPelA is a metal-dependent CE enzyme with α-1,4-N-acetylgalactosaminidase activity

Previous studies of *Pa*PelA, its isolated hydrolase domain, and variants thereof have demonstrated that the enzyme exhibits esterase activity and is an α-1,4-*N*-acetylgalactosaminidase (18, 19, 43, 44). To confirm that *Pt*PelA is an active enzyme, we first probed for esterase activity using the pseudo-substrate acetoxymethyl-4-methylumbelliferone (AMMU) (44, 45). As anticipated, titration of AMMU into 1 μM of WT *Pt*PelA resulted in a concentration-dependent increase in esterase activity (Fig. S3).

As CE4 and CE18 enzymes require a divalent cation to stabilize the oxyanion tetrahedral intermediate during deacetylation (34, 35), we next sought to determine if *Pt*PelA's esterase activity was dependent on residues implicated in metal binding from our structural comparisons with well-characterized metal-dependent CE4 and C18 enzymes. We first assessed the esterase activity of the WT protein and four alanine point mutants, including residues D517, D519, H589, and H593 (residues D528, D530, H600, and H604 in *Pa*PelA).

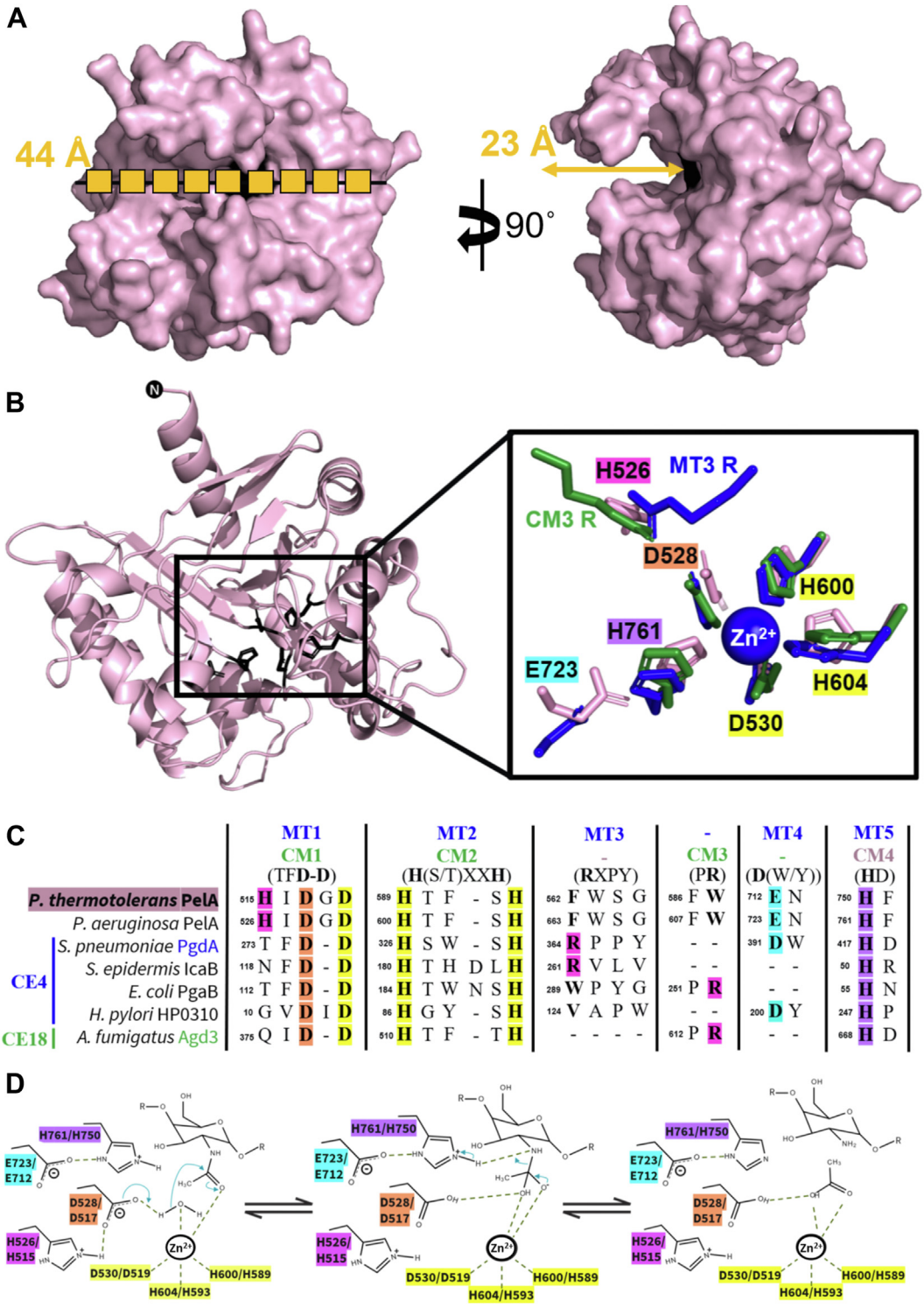

Figure 2. PelA is the founding member of a novel CE family. *A*, surface representation of the AF2 model of *Pa*PelA from two opposing views. The polymer in the first view of *Pa*PelA is representative of nine GalNAc residues (38). *B*, the *Pa*PelA^{AF2} deacetylase domain (*left*). Inset of a structural alignment of the catalytic residues of *Pa*PelA (*pink*) with representative CE4 and CE18 enzymes: *Streptococcus pneumoniae* PgdA (2C1G, *blue*) and *Aspergillus fumigatus* Agd3 (6NWC, *green*), respectively. The zinc that cocrystallized with *Sp*PgdA is shown as a *blue sphere*. *C*, primary sequence alignment of the catalytic motifs MT1-5 and CM1-4 characteristic of CE4 and CE18 enzymes, respectively, as determined by structural alignment. The putative *Pa*PelA catalytic base (D528), metal coordinating triad (D530, H600, and H604), and putative catalytic acid (H761) are highlighted in *orange*, *yellow*, and *purple*, respectively. The aspartate that coordinates the catalytic acid (E723) and the histidine that is proposed to coordinate the catalytic base (H526) is shown in *cyan* and *pink*, respectively. *D*, proposed metal-dependent de-*N*-acetylation reaction for *Pa*PelA (first listed amino acid) and *Pt*PelA (second listed amino acid) based on the mechanisms for CE4 and CE18 enzymes and mutagenesis data.

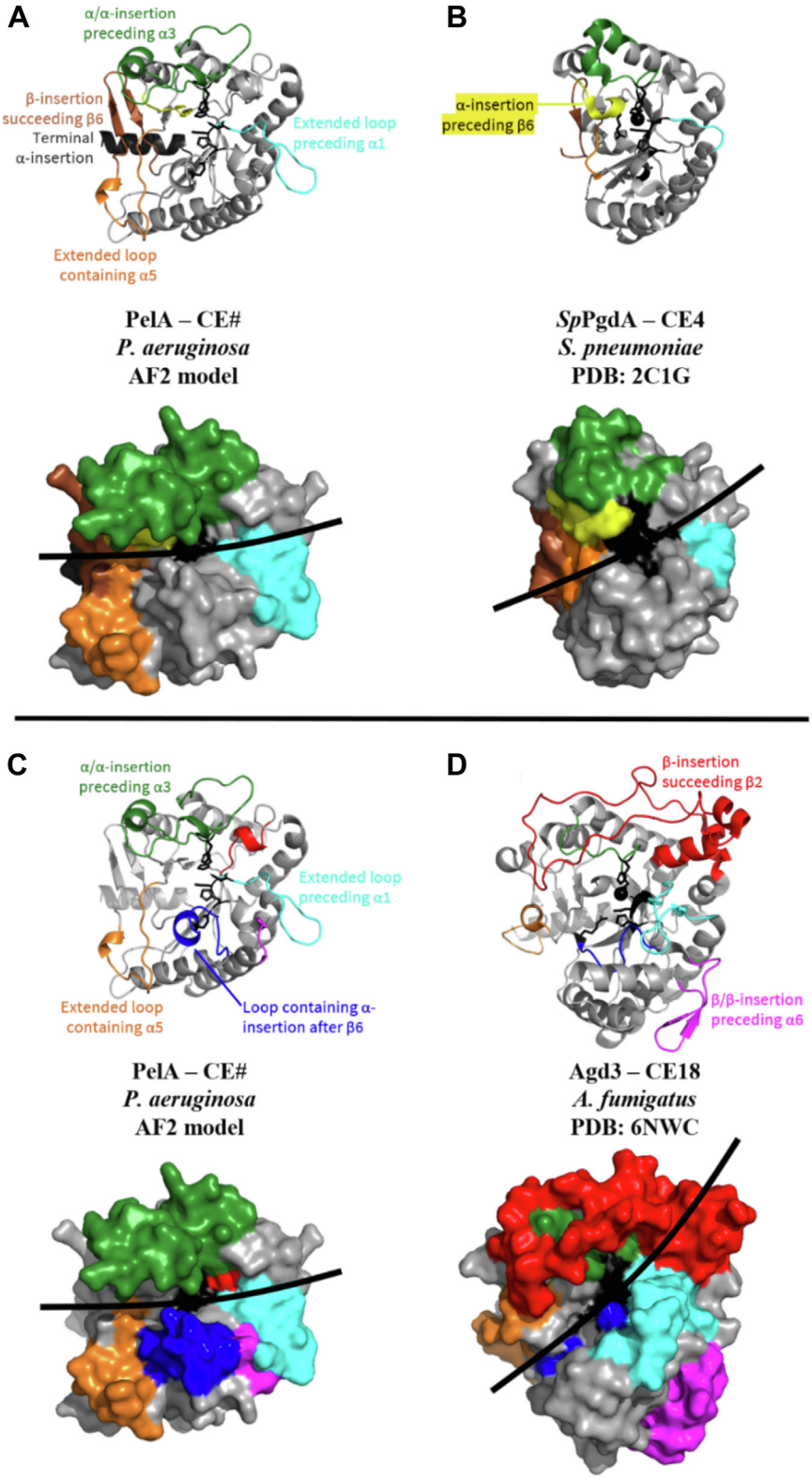

Figure 3. *Pt*PelA has structural differences in comparison to CE4 and CE18 enzymes. *A* and *B*, cartoon and surface representations to compare the AF2 model of *Pa*PelA (*A*) and the structure of *Sp*PgdA (*B*). Regions where there are major structural differences are colored and labeled accordingly. Active site residues are shown in *black*. The *black lines* highlight the active site grooves. *C* and *D*, cartoon and surface representations to compare the AF2 model of *Pa*PelA (*C*) and the structure of Agd3 (*D*).

No detectable esterase activity was observed with any of the mutants (Fig. 4*A*), suggesting that a divalent metal is required and implicating D517 (residue D528 in *Pa*PelA) as the putative catalytic base. Differential scanning fluorimetry revealed each of the mutants, with the exception of the H593A mutant, has comparable stability to the WT protein, suggesting that the

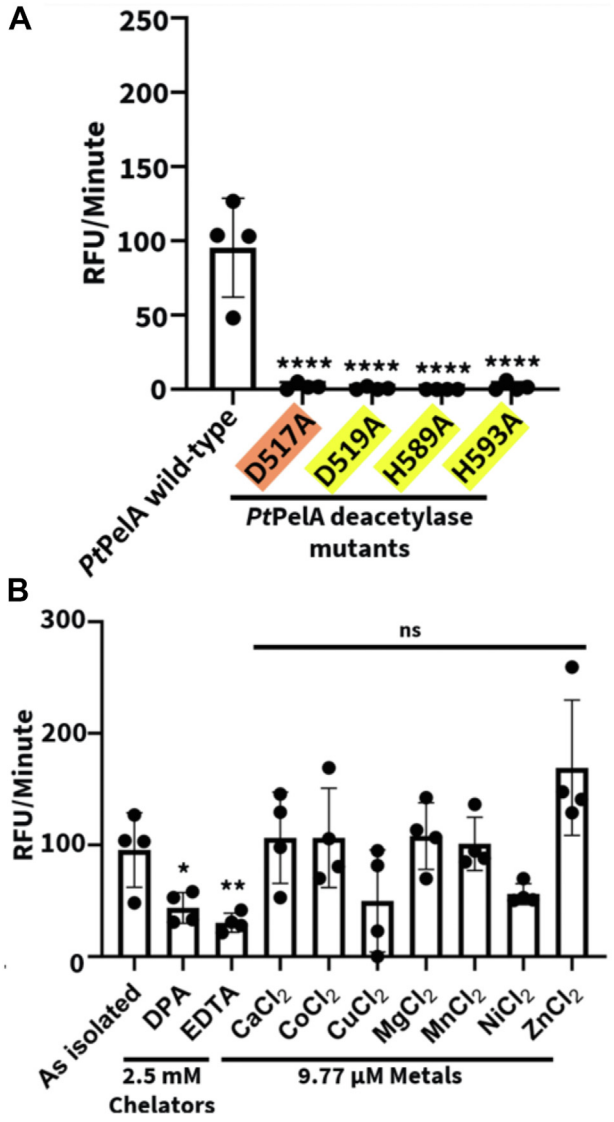

Figure 4. *Pt*PelA is a metal-dependent CE21 enzyme. *A*, detection of WT or mutant *Pt*PelA esterase activity using the AMMU pseudosubstrate. The putative catalytic base and metal coordinating triad are highlighted in *orange* and *yellow*, respectively. Statistical significance was calculated using an ordinary one-way ANOVA with Dunnett's multiple comparison test between WT and mutant *Pt*PelA. The error bars show the SEM for the four independent assays with two technical replicates. ****$p < 0.0001$; **$p < 0.0021$; *$p < 0.0332$; ns, not significant. *B*, detection of *Pt*PelA metal-dependent esterase activity using the AMMU substrate. Statistical significance was calculated using a one-way ANOVA with Dunnett's multiple comparison test between *Pt*PelA as isolated and the other reaction conditions with chelator or metal chloride. AMMU, acetoxymethyl-4-methylumbelliferone.

changes observed in activity are not due to loss of stability (Table S1). Next, we pre-incubated the WT protein with a range of metal chelators or the chloride salts of divalent cations and performed the AMMU esterase assay to determine the preferred metal (Fig. S4) (22, 34). While the addition of the dipicolinic acid or ethylenediaminetetraacetic acid metal chelator resulted in a significant 2-fold reduction of esterase activity, *Pt*PelA still retained low levels of esterase activity even at the highest concentration tested (Fig. 4*B*). At 9.77 μM of metal, which is comparable to the concentration reported in previous studies of CE4 enzymes (34, 35) and represents a 1:10 M excess of protein:metal in the current studies, exogenous addition of all tested metals did not have a significant effect. However, there was a trend towards increased activity with the addition of Zn^{2+}, a metal commonly predicted to be used by CE4 enzymes (Fig. 4*B*) (34, 35, 46–49). Given the recent availability of AlphaFold3 (AFCE3), which allows for the modeling of select ions, we also predicted the structure of *Pa*PelA with Zn^{2+} and Mn^{2+}, two commonly used CE4 metals (50). We found that in both cases, the ion was predicted to be coordinated by D530, H600, and H604 residues (Fig. S3, *B* and *C*). Collectively, these results suggest that D530, H600, and H604 are required for PelA esterase activity and that these residues likely bind Zn^{2+}.

Having confirmed that *Pt*PelA has esterase activity, we next sought to determine using a biofilm disruption assay whether the protein exhibited α-1,4-*N*-acetylgalactosaminidase activity (19, 43). Using *P. aeruginosa* PA14, which produces a Pel-dependent biofilm, we found that *Pt*PelA could disrupt preformed biofilms with a half-maximal effective concentration (EC_{50}) of 78.5 ± 0.7 nM (Fig. 5, *A* and *B*). This is comparable to the EC_{50} for the recombinant hydrolase domain of *Pa*PelA (*Pa*$PelA_H$) (88.3 ± 0.9 nM) (43). Alanine point mutants of residues required for *Pt*PelA hydrolase activity, D149 and E207, cannot disrupt the biofilms (Fig. 6, *A* and *B*). To confirm these results, we assessed *Pt*PelA's ability to hydrolyze a pool of α-1,4-GalNAc oligosaccharides. Digestion of this pool of oligosaccharides, which ranged from 5-mer (m/z = 1056.393 ± 0.05) to 15-mer (m/z = 3087.110 ± 0.10) (Fig. 5*C*) (14, 19), was analyzed using matrix-assisted laser desorption/ionization-time of flight (MALDI-TOF) mass spectrometry (MS). Consistent with the results of the disruption assay, we observed a shift in the size range of the initial sample. After *Pt*PelA treatment, the oligosaccharides size ranged from 3-mer (m/z = 650.439 ± 0.07) to 11-mer (m/z = 2274.803 ± 0.10) (Figs. 5*C* and S5).

Together, these results reveal that *Pt*PelA, like *Pa*PelA, exhibits both esterase and α-1,4-*N*-acetylgalactosaminidase activity and that given the low sequence identity to existing CE families, the PelA deacetylase domain is the founding members of a new CE family, CE21 (33).

*Pa*PelA CE function is regulated by *Pa*PelB

We have previously shown that interaction with *Pa*PelB increases *Pa*PelA's esterase activity in a *p*-nitrophenol assay and attenuates the hydrolysis of a preformed Pel-dependent *P. aeruginosa* biofilm (21). We hypothesized that the PelAB interaction results in less hydrolysis of Pel in the *P. aeruginosa* biofilm due to a potential increase in deacetylation. However, whether the presence and absence of PelB alters how PelA modifies Pel has not been characterized.

Given that *Pt*PelA has comparable esterase and hydrolase capabilities to *Pa*PelA (19, 43, 44), to be consistent with our previous studies, and given the availability of *Pa*PelA and *Pa*PelB constructs, our subsequent analysis focused on the *P. aeruginosa* enzymes. To examine both deacetylation and hydrolysis simultaneously and the effect PelB may have, a mix of purified α-1,4-GalNAc oligosaccharides of various lengths was

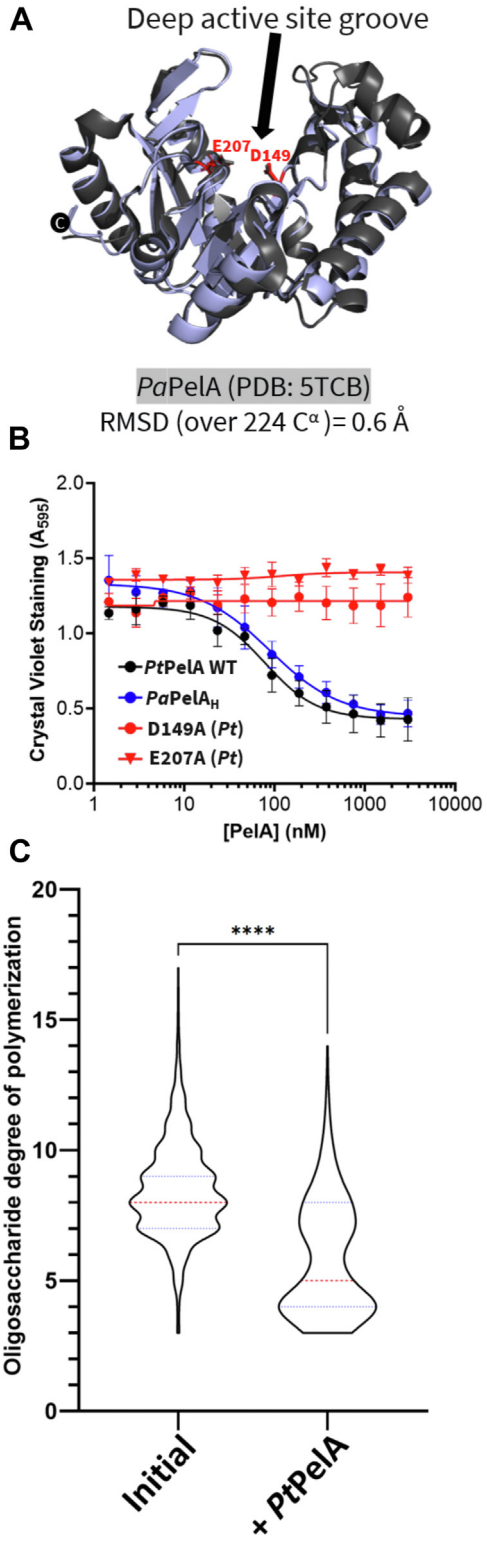

Figure 5. *Pt*PelA has α-1,4-*N*-acetylgalactosaminidase activity. *A*, structural comparison of the hydrolase domain of *Pt*PelA (*blue*) with the hydrolase domain of *Pa*PelA (5TCB, *gray*). Amino acids required for the hydrolase activity of *Pt*PelA (D149 and E207) and *Pa*PelA are shown in *red* and *gray*, respectively. *B*, a biofilm disruption assay. Increasing concentrations of WT *Pt*PelA (*black circle*), *Pa*Pela$_H$ (*blue circle*), or *Pt*PelA hydrolase domain mutants D149A (*red circle*) or E207A (*red triangle*) were added to preformed PA14 Pel biofilms. The error bars show the SEM for the average of three technical replicates in three independent assays. *C*, population statistical study of the MALDI-TOF MS enzyme spectra of the oligomers released due to hydrolysis after incubating WT *Pt*PelA. The data represent three biological replicates each with three technical replicates. Statistical significance was calculated using a one-way ANOVA with Dunnett's multiple comparison test between the indicated reaction conditions. ****$p < 0.0001$. The median size of the oligosaccharides is shown by the *dotted red line*. The 25th and 75th quartiles are shown by the *blue dotted lines*, respectively.

added to 1 μM *Pa*PelA in the presence or absence of a soluble construct of *Pa*PelB that includes the TPRs and α-rich region that precedes the β-barrel porin domain (residues 47–880). The previously reported *Pa*PelA:*Pa*PelB ratio of 1:1.5 was used in the MALDI-TOF MS experiments (21). We monitored the potential hydrolysis and/or deacetylation reaction products over three time points. As the minimum substrate length for hydrolysis to occur is a heptamer (19), the relative ion proportion of the trimer to hexamer population was monitored and recorded as the reaction products. Only a minor amount of 5- and 6-mer was present in the initial sample (Fig. 6*A*). Incubation of the oligosaccharide mixture with *Pa*PelB did not alter the ion relative proportion of the end products (Figs. 6*A* and S6). In contrast, incubation with 1 μM of *Pa*PelA resulted in a constant increase in the trimer to hexamer product population (Fig. 6*A*). Addition of *Pa*PelB did not significantly change the population of hydrolysis products produced at any of the time points (Fig. 6*A*). We also tested the isolated hydrolase domain of *Pa*PelA (*Pa*PelA$_H$) under similar conditions. Use of *Pa*PelA$_H$ led to a similar increase in the 3- to 6-mer product population as observed with the full-length enzyme (Fig. 6*B*). Our results indicate that interaction with *Pa*PelB does not affect the hydrolase activity of *Pa*PelA or the isolated *Pa*PelA$_H$ domain under the conditions tested.

Under the conditions of the experiment, no oligosaccharide deacetylation was observed. The initial oligosaccharide sample contained a small (<3%) population of GalN residues (Fig. S6*A*), and as anticipated, this population did not change upon incubation with *Pa*PelB. However, in the presence of both *Pa*PelA and *Pa*PelAB, hydrolysis of the oligosaccharide leads to the loss of detectable GalN structures above the background noise of the spectra. As this data suggested that the deacetylase activity is slower than hydrolysis under the conditions tested, we generated a double hydrolase-inactivated mutant, *Pa*PelA$^{\Delta DH}$ (D160A E218A), to explore deacetylase activity. Using this enzyme, deacetylation events could be observed when 15 μM enzyme was incubated with the oligosaccharides for 24 h. As *Pa*PelB is not stable when concentrated to 22.5 μM, we were unable to use the same 1:1.5 *Pa*PelA:*Pa*PelB ratio we used previously to examine the hydrolysis reaction and opted for a *Pa*PelA:*Pa*PelB ratio of 1.5:1. To determine the minimal length substrate required for deacetylation, the α-1,4-GalNAc oligosaccharides substrate mixture was incubated with *Pa*PelA$^{\Delta DH}$. We found that the longer oligosaccharides are partially deacetylated (Fig. 6*C*). The shortest substrate that was affected by *Pa*PelA$^{\Delta DH}$ was a pentamer (Fig. 6*D*). The frequency and relative proportion of deacetylation events increased with oligosaccharide length. In contrast to the observed hydrolase activity, adding even a substoichiometric amount of *Pa*PelB to *Pa*PelA$^{\Delta DH}$ enhanced its deacetylase activity (Fig. 6*E*). While the minimal substrate

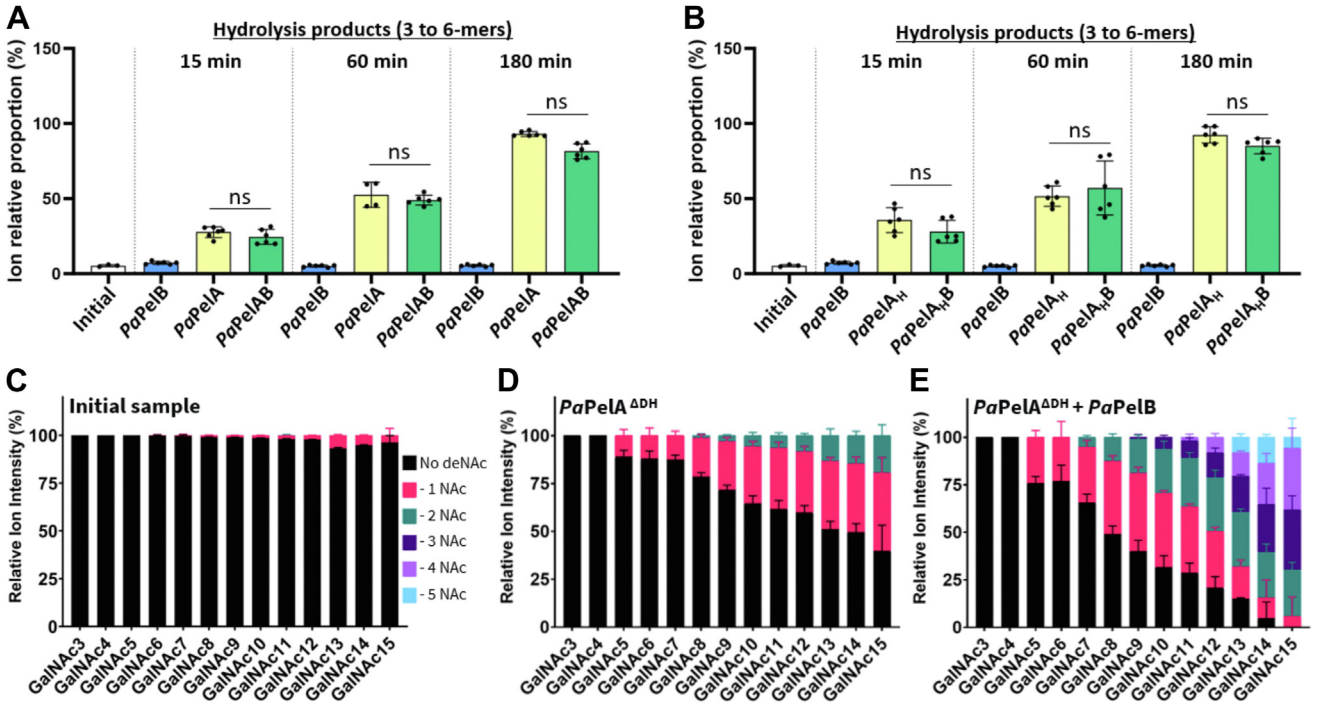

Figure 6. Interaction with *Pa*PelB does not affect *Pa*PelA hydrolase activity but increases the deacetylation of α-1,4-GalNAc oligosaccharides by *Pa*PelA. *A* and *B*, the ion relative proportion of the MALDI-TOF MS enzyme spectra of the 3 to 6-mer oligomers released due to hydrolysis after incubating WT *Pa*PelA (*A*) or *Pa*PelA$_H$ (*B*) in the absence or presence of *Pa*PelB. The data represent three biological replicates each with two technical replicates. Statistical significance was calculated using Kruskal–Wallis multiple comparison tests between the indicated reaction conditions. *C–E*, MALDI-TOF MS analysis of the deacetylation products for the oligosaccharides in isolation (*C*) and after incubating *Pa*PelA^{DH} in the absence (*D*) or presence (*E*) of *Pa*PelB. Ns, not significant.

length required for deacetylation did not change, a marked increase in the relative proportion of oligosaccharide being deacetylated and the frequency of deacetylation events was observed (Fig. 6*E*). Tandem mass spectrometry structural characterization of select deacetylated oligosaccharides was unable to reveal the exact position of the deacetylation events, highlighting the heterogeneity of the oligosaccharide processing by *Pa*PelA *in vitro* (Fig. S7, *B* and *C*). However, despite our inability to locate the first deacetylation event, it is important to note that the addition of *Pa*PelB did not alter the tandem mass spectrometry fragmentation trace obtained, demonstrating that the addition of *Pa*PelB did not modify how *Pa*PelA processes the oligosaccharides (Fig. S7, *B* and *C*). Collectively, these results suggest that *Pa*PelB can directly affect the rate of deacetylase activity without changing the fundamental properties of minimal substrate length or sites of deacetylation.

Full-length homologs of PelA are present in many Gram-negative bacterial phyla

When submitting the structure of *Pt*PelA to the DALI server, only structures of the isolated hydrolase or deacetylase domains of enzymes were identified (29). These results suggest that the domain organization in the full-length structure of *Pt*PelA is unique with respect to experimentally solved structures. As the AF2 database provides us with an opportunity to search for structural models of PelA homologs across all phyla, we next ran a nonredundant tertiary structure similarity search of *Pa*PelA^{AF2} using FoldSeek (Table S2.1) (51). We identified full-length homologs in 96 bacterial species with >85% amino acid coverage and >45% sequence similarity using ClustalW. We also searched a nonredundant database for homologs of *Pa*PelA using BLASTP (52), which searches based on sequence similarity. BLASTP identified 177 bacterial species with >85% amino acid coverage and >38% sequence similarity (Table S2.2). Aside from one Gram-positive species, all full-length homologs of *Pa*PelA identified in our FoldSeek and BLASTP searches were from Gram-negative species.

The sequences of *Pa*PelA and the homologs identified using FoldSeek were used to generate a maximum likelihood tree in Geneious, which identified 16 different bacterial phyla (Fig. 7*A*). One-third of hits were in the gammaproteobacterial phylum that *P. aeruginosa* and *P. thermotolerans* are a part of (Table S3). Betaproteobacterial species such as *Neisseriaceae*, *Ralstonia*, and *Cupriavidus* contained about one-fourth of the full-length *Pa*PelA homologs. While four of the sequences came from unclassified phyla, most of the other sequences came from the aquificota, epsilonproteobacteria, and verrucomicrobiota phyla (Table S3). Interestingly, the homologs identified using BLASTP only identified eight unique bacterial phyla, with 33% and 63% of the hits corresponding to the betaproteobacterial and gammaproteobacterial phyla, respectively.

Using BioCyc, we found that only 21% (20/96) and 43% (76/177) of the *Pa*PelA homologs identified using FoldSeek

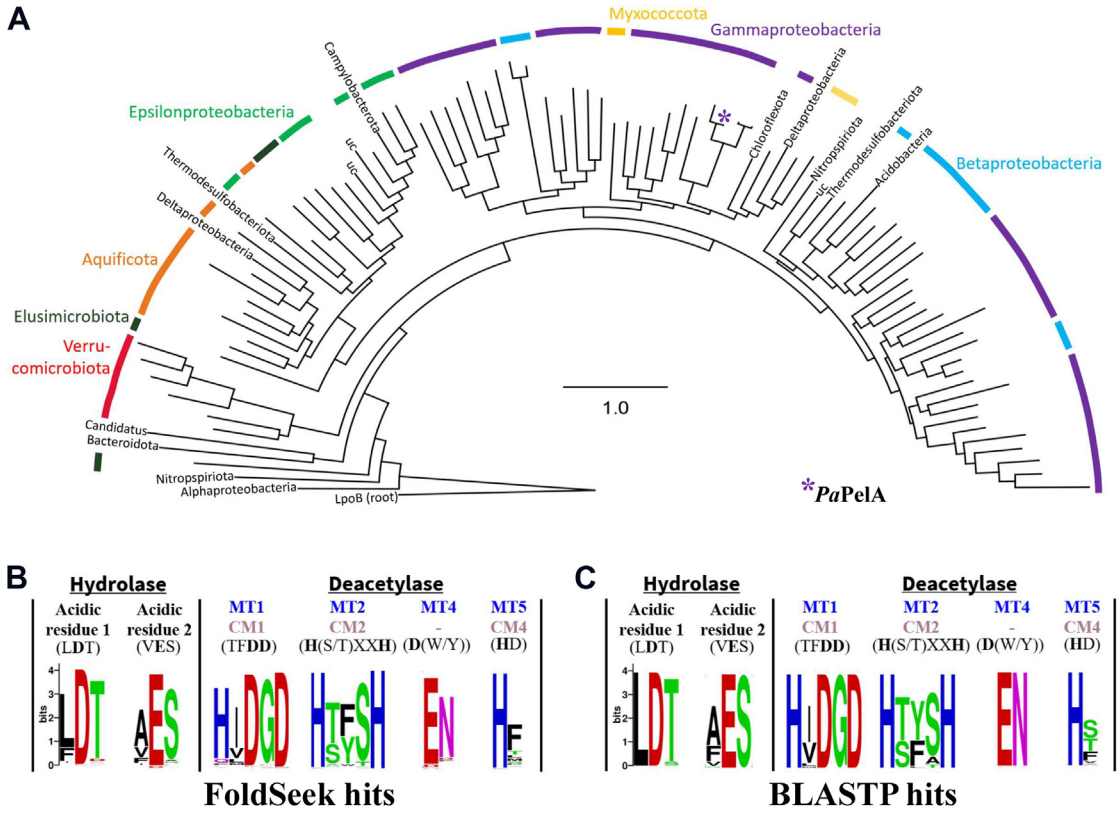

Figure 7. Full-length PelA is distributed across multiple Gram-negative phyla and has conserved active site residues. *A*, phylogenetic distribution of PelA among bacterial taxa. The circular tree represents the approximately-maximum-likelihood distance between 96 unique PelA sequences, which was constructed using FastTree and *Escherichia coli* LpoB as an outgroup. PelA sequences were identified by running a FoldSeek search of *Pa*PelA. *B* and *C*, multiple sequence alignment of *Pa*PelA homologs identified through FoldSeek (*B*) or BLASTP (*C*) and visualized using WebLogo 3. The catalytic motifs MT1-5 and CM1-4 are characteristic of CE4 and CE18 enzymes.

and BLASTP, respectively, were linked to a *pelABCDEFG* operon. The FoldSeek and BLASTP data resulted in the identification of eight and seven new species, respectively, with *pel* or *pel*-like operons that had not been identified in our previous phylogenetic analyses (Table S4) (53). Considering that 5% and 44% of the *Pa*PelA homologs identified using FoldSeek and BLASTP were in unclassified species for which full genomic information is unavailable, it is likely that more of these homologs may be in *pel* or *pel*-like operons. While the genomic context for many of the homologs identified in our searches is not available, every PelA homolog that we could search the genome for is in a *pel* operon. This strongly suggests all of the PelA homologs are probably associated with *pel* operons. Alignment of *Pa*PelA to its full-length homologs revealed conservation of the hydrolase and deacetylase active site amino acids with only minor differences occurring in the logos obtained from our FoldSeek and BLASTP data sets (Fig. 7, *B* and *C*). Due to the high degree of structural conservation, these results suggest that the hydrolase and deacetylase activities of the full-length PelA homologs could be essential in bacterial species that contain the *pel* operon. Additional work will be needed to determine if the *pel* operons are functional and if the PelA–PelB interaction remains relevant in these less-studied organisms.

AF2 PaPelAB complex predicts PelA's deacetylase and mixed α/β domains interact with PelB

We have previously shown that the outer membrane localization of *Pa*PelA and Pel-dependent *P. aeruginosa* biofilm formation require TPRs 9 to 14 of *Pa*PelB (21). We also demonstrated *via* copurification using size-exclusion chromatography that while full-length *Pa*PelA interacts directly with a *Pa*PelB protein construct containing TPRs 9 to 14, the isolated hydrolase domain of *Pa*PelA, $Pa\text{PelA}_H$, does not (21). To provide additional insight into which domain(s) of *Pa*PelA could be important for interacting with *Pa*PelB, we generated AF2 models of *Pa*PelB and the *Pa*PelAB complex (Fig. S8*A*). Of note, AF3 produced the same *Pa*PelAB and *Pa*PelAB models, with the exception of a kink after the eighth TPR of *Pa*PelB (50).

Examination of the AF2 *Pa*PelB structure and bioinformatics analyses suggest that amino acids 1 to 36 form an inner membrane α-helix rather than the hypothesized signal sequence (Fig. S8*B*) (21). As anticipated, amino acids 69 to 726 and 876 to 1193 encompass TPRs 1 to 19 and the β-barrel porin domain, respectively (Fig. 8*A*). The previously determined crystal structure of *Pa*PelB, which includes TPRs 8 to 11, aligns well to the AF2 model of *Pa*PelB (21). While amino acids 37 to 68 and 727 to 910 were previously predicted to be unstructured regions (21), the AF2 model predicts with low

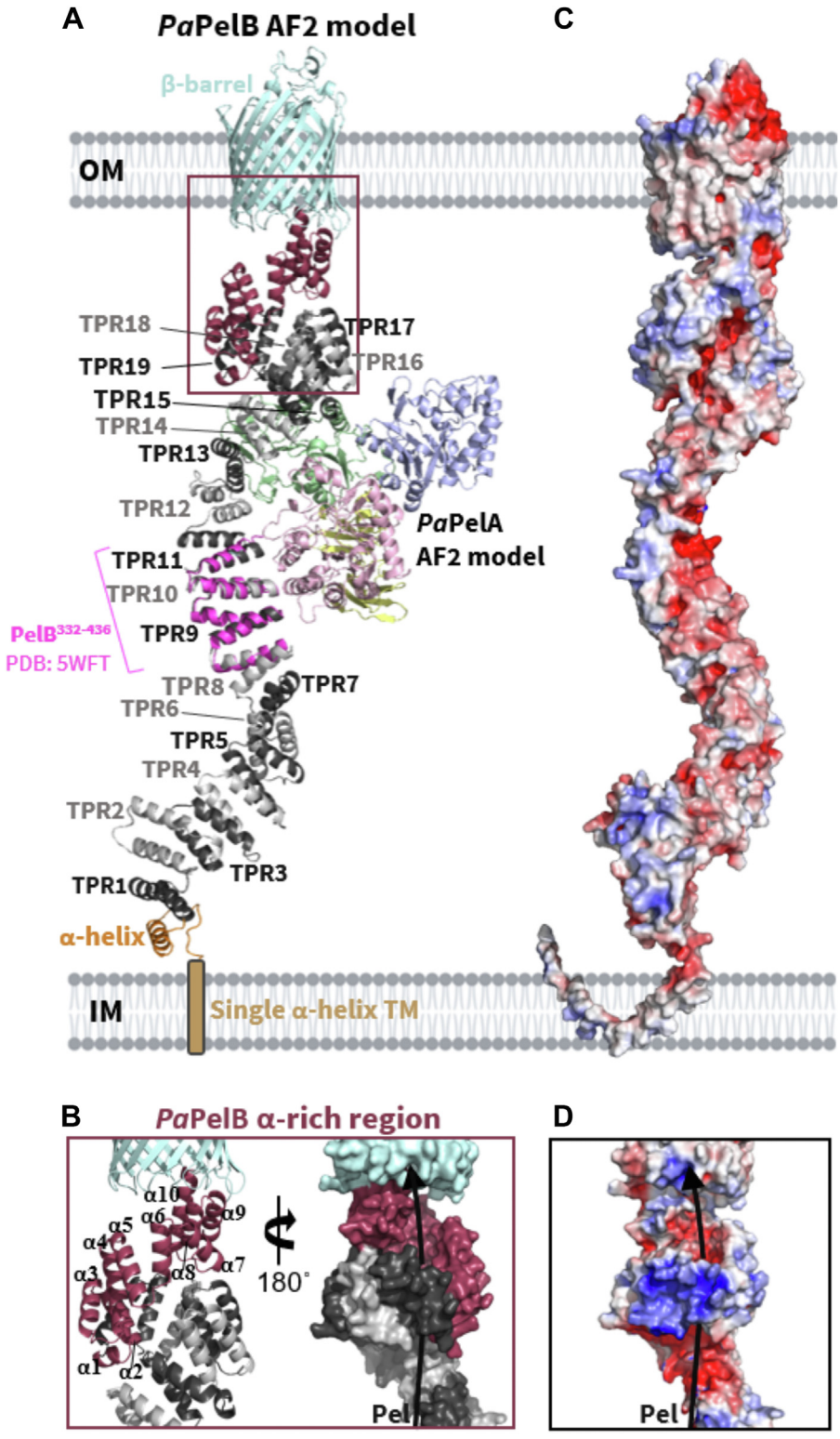

Figure 8. Structural models of *Pa*PelB, *Pa*PelC, and the *Pa*PelBC complex. *A*, AF2 model of full-length *Pa*PelB complexed with *Pa*PelA (colored by domains as in Fig. 1). *Pa*PelB is colored by domain and aligned to the structure of *Pa*PelB$^{332-436}$ (5WFT, *magenta*). *B*, the α-rich region of *Pa*PelB from two opposing views. The *black arrow* indicates the proposed trajectory of Pel through PelB. *C*, electrostatic surface representation of *Pa*PelB calculated by APBS in PyMol and visualized from −5 (*blue*) to 5 (*red*) kT/e. *D*, electrostatic surface representation of the α-rich region of *Pa*PelB.

confidence a single α-helix and an α-rich region for these residues, respectively (Figs. 8*A* and S8*B*). The ten α-helices in the α-rich region do not form canonical ∼34-amino acid long TPR pairs (54), but they do supercoil and form an electronegative portal that leads to the β-barrel porin domain (Fig. 8, *B–D*).

In keeping with our previous data that had shown that TPRs 9 to 14 of *Pa*PelB are required for the outer membrane

localization of *Pa*PelA (21), the AF2 model of the PelAB complex predicts an interaction between the deacetylase domain of *Pa*PelA and TPRs 9 to 15 of *Pa*PelB (Fig. 8*A*) (21). The mixed α/β domain of *Pa*PelA is also predicted to interact with TPRs 13 to 19 of *Pa*PelB. This suggests that the function of the mixed α/β domain of PelA is likely to help coordinate *Pa*PelAB complex formation. In the AF2 *Pa*PelAB model, the hydrolase and β-rich domains of *Pa*PelA do not interact with *Pa*PelB (Fig. 8*A*).

Model showing the projected path of Pel through the PaPelABC complex

To gain insight into how Pel is modified and exported, we next built a composite model of the *Pa*PelABC complex by combining our PelAB AF2 model and generating the PelBC AF2 model (Fig. 9*A*). While this *Pa*PelABC complex remains to be experimentally validated, a preprint of the cryo-EM co-structure of the PelB α-rich and β-barrel OM domains with full-length dodecameric PelC was recently published (55). This *Pa*PelBC structure lacks the TPR domain of PelB (PelB^{-TPR}C). As the coordinates of the PelB^{-TPR}C structure have not been released, we examined the figures presented therein and found that our previously published dodecameric *Paraburkholderia phytofirmans* PelC (*Pp*PelC) crystal structure (20) is comparable to PelC in both the PelB^{-TPR}C costructure and our PelABC AF2 model. In both models, PelC encloses the α-rich domain of PelB.

Our *Pa*PelABC model suggests that after synthesis and translocation of the polymer across the cytoplasmic inner membrane by PelDEFG, Pel would interact with TPRs 1 to 9 of PelB. This interaction helps guide the polymer through the periplasmic space and delivers it to PelA. The *Pa*PelA–*Pa*PelB interaction orients the deacetylase domain to readily bind to the fully acetylated GalNAc polysaccharide. The interaction of PelB and PelA *via* TPR 9 to 15 exposes an electronegative groove that we propose guides the now positively charged, partially deacetylated product towards the outer membrane (Fig. 8, *C* and *D*). Intriguingly, if the polymer follows this path, it will not be exposed to the hydrolase domain (Fig. 9, *B* and *C*). The model also shows that PelA and PelC do not interact and that PelC is therefore unlikely to affect PelA function. The interaction of the dodecameric lipoprotein PelC with PelB in both the PelB^{-TPR}C costructure and our PelABC AF2 model supports our previous hypothesis that PelC acts as an electrostatic funnel to attract cationic Pel and to guide it toward the PelB's porin domain for export (20).

Discussion

In this study, we present the structural characterization of the Pel polysaccharide modification enzyme, PelA. We determined the crystal structure of PelA from *P. thermotolerans* to 2.1 Å, revealing a unique four-domain architecture (Fig. 1). Bioinformatics analyses of *Pseudomonas* PelA homologs reveal

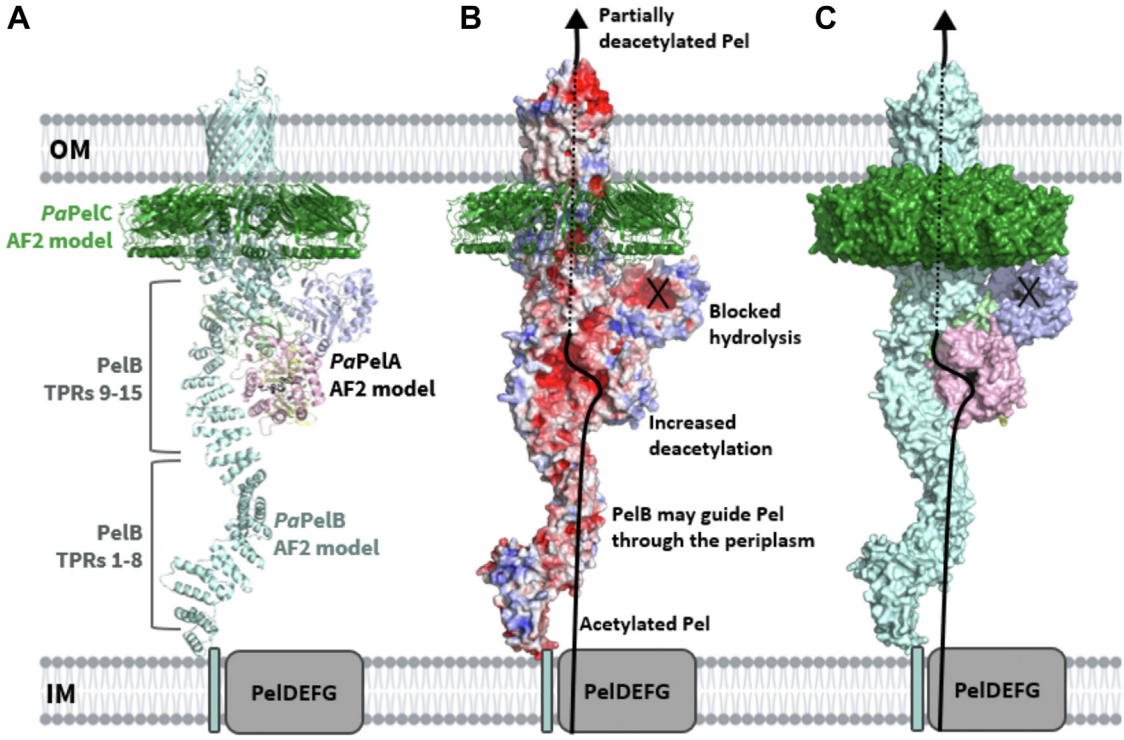

Figure 9. Model of the *Pa*PelABC outer membrane Pel modification and secretion complex. *A*, AF2 model of full-length *Pa*PelB (*light cyan*) complexed with *Pa*PelA (colored by domains as in Fig. 1). AF2 model of amino acids 600 to 1193 of *Pa*PelB complexed with the 12-subunit ring of *Pa*PelC (*green*) were aligned to the *Pa*PelAB complex prediction. The fragment of *Pa*PelB used for the *Pa*PelBC prediction was then excluded from this figure. *B*, cartoon representation of dodecameric *Pa*PelC and the surface representation of *Pa*PelAB from (*A*) as colored by electrostatics, which were calculated by APBS in PyMol and visualized from −5 (*blue*) to 5 (*red*) kT/e. The *solid black line* indicates the proposed trajectory of Pel export while *Pa*PelA and *Pa*PelB interact. The *dotted black line* indicates when the polymer is enclosed by the pore formed by the *Pa*PelAB complex. *C*, surface representation of (*A*). The active site amino acids of the deacetylase and hydrolase domains of *Pa*PelA are shown in *black*.

conservation of the catalytic residues and predicted structures (Table S2 and Fig. 7), suggesting that PelA modifies a GalNAc-rich polysaccharide in bacterial species that contain a *pel* operon. Using sequence analysis and enzymatic assays, we found that *Pt*PelA and its homologs define a new class of carbohydrate esterases, CE21, with distant homology to the CE4 and CE18 families (Figs. 2–4). Importantly, we show using MALDI-TOF MS that the interaction of *Pa*PelA with *Pa*PelB results in increased deacetylation of α-1,4-GalNAc oligosaccharides (Fig. 6, *C–E*) but does not directly affect the proportion of hydrolytic products (Fig. 6, *A* and *B*).

Deacetylation of exopolysaccharides is an important modification in Gram-negative and -positive bacterial biofilms (22, 35–37). *Pa*PelA deacetylase activity is essential for biofilm formation, as chromosomal mutation of deacetylase active site residues in *P. aeruginosa* PA14 results in impaired biofilm formation (18). Using a 1:10 protein:metal concentration in the AMMU assay (Fig. 4*B*), we did not find a metal that significantly increased *Pt*PelA's esterase activity. While CE4 and CE18 enzymes require metals for their mechanism of action, they are often promiscuous in their metal dependency (22, 33–35, 50, 51). As many CE4 enzymes are zinc-dependent and/or have been cocrystallized with zinc, and there is a trend toward increased esterase activity in the presence of zinc under the conditions tested in the AMMU assay (Fig. 4*B*), zinc likely enhances the deacetylase activity of *Pa*PelA *in vivo* (22, 34–36, 56, 57). It is also important to note that, as *P. aeruginosa* and *P. thermotolerans* reside in different environmental niches, the metal utilized by *Pa*PelA may vary from the results seen for *Pt*PelA (58, 59).

*Pa*PelA lacks the mostly conserved arginine in the MT3 and CM3 active site motifs of CE4 and CE18 enzymes, respectively (Fig. 2, *B* and *C*). In CE4 and CE18 family members, this arginine is proposed to activate the aspartate that functions as the catalytic base. There is some variation across CE4 enzymes regarding the location of this arginine in the primary sequence and the orientation it adopts in the active site. For example, compared to *Sp*PgdA, the conserved arginine in *Escherichia coli* PgaB is positioned in the CM3 motif that is characteristic of CE18 enzymes and is oriented differently in the active site with respect to the catalytic base from MT1 (22). The activating arginine residue appears to be required for activity in CE4 family members. *Hp*PgdA (60), which does not have an arginine residue in its active site, did not show activity on the *N*-acetylated polysaccharides that are typically used by peptidoglycan deacetylases under the conditions tested (35, 60, 61). While *Pt*PelA and *Pa*PelA lack the arginine that activates the catalytic base in CE4/CE18 enzymes, our analysis reveals that they are active deacetylases. Examination of the *Pt*PelA structure and bioinformatic analyses of the PelA homologs identified using FoldSeek and BLASTP suggest that the conserved histidine in the MT1/CM1 performs this function. Except for this difference in the residue that activates the catalytic base, *Pa*PelA has all of the CE4/CE18 consensus residues in its active site motifs. We propose a mechanism for *Pa*PelA and CE21 enzymes wherein the water that is coordinated by a divalent cation is deprotonated by the catalytic base, D528 (Fig. 2*D*). The resulting nucleophile then attacks the acetate group of acetylated Pel, generating an oxyanion tetrahedral intermediate that is stabilized by the divalent cation. The catalytic acid, H750, then donates a proton to the intermediate, releasing acetate from Pel (Fig. 2*D*).

Our previous studies showed that full-length *Pa*PelA, but not the isolated hydrolase domain, interacts with *Pa*PelB (21). The AF2 prediction of the *Pa*PelAB complex supports these data, as only the deacetylase and mixed α/β domains of *Pa*PelA are involved in the interaction interface (Fig. 9). As AF2 is unable to predict conformational changes, the current AF2 model only enables a mechanism for the deacetylation of Pel to be predicted. In *E. coli*, the dual-active protein PgaB first partially deacetylates the PNAG polymer (26). Deacetylated PNAG is then predicted to wrap around PgaB until it encounters the hydrolase domain before being exported by the OM protein PgaA (26). It is, therefore, possible that a shift in the mixed α/β and/or deacetylase domains of *Pa*PelA could alter the binding groove of the protein such that hydrolysis can occur. While it is unclear whether the structure of *Pa*PelB is rigid, it is also possible that *Pa*PelB can undergo conformational changes in response to periplasmic stress or from an unknown interaction partner, which could ultimately affect how the protein interacts with *Pa*PelA. Consequently, our previous studies and the *in vitro* functional studies presented herein of the *Pa*PelAB complex may not account for the conditions that would favor a different conformational state. As the hydrolase domain is important for generating the cell-free form of Pel and thus controls biofilm biomechanics and plays a role in modulating *P. aeruginosa* virulence, future work is required to understand if there are conditions under which hydrolysis is activated. Furthermore, future studies determining the cryo-EM structures of the *Pa*PelAB and *Pa*PelABC complexes in the presence and absence of Pel will be required to understand how *Pa*PelA can deacetylate and hydrolyze the polymer before secretion from the cell.

While we found that the *Pa*PelAB interaction increased deacetylation of α-1,4-GalNAc oligosaccharides (Fig. 6, *C–E*), it is important to keep in mind that hydrolysis of α-1,4-GalNAc oligosaccharides dominates over deacetylation *in vitro* and that the *Pa*PelAB complex may not bind the full-length Pel polymer in the same way during biosynthesis. Despite our previously published findings that the addition of *Pa*PelB increased the hydrolytic activity of *Pa*PelA in a preformed biofilm disruption assay, *Pa*PelB did not affect the hydrolysis of α-1,4-GalNAc oligosaccharides (Fig. 6, *A* and *B*). While the substrate for *Pa*PelA in the preformed *P. aeruginosa* biofilm contained partially deacetylated Pel, fully acetylated oligosaccharides were used as the substrate in the MALDI-TOF experiments herein. Therefore, it is likely that the acetylation state of Pel affects how the PelAB interaction regulates hydrolysis. This data supports our previous study showing that $Pa\text{PelA}_{H}$ hydrolyzes acetylated Pel more easily than mature, partially deacetylated Pel (14). Alternatively, it is possible that additional interaction partners or different conditions would be required to elicit a change in the hydrolysis of Pel by *Pa*PelA and its interaction with *Pa*PelB.

Despite being less efficient than the hydrolase domain, the deacetylase domain of *Pa*PelA likely acts on the Pel polysaccharide first since Pel is likely guided directly to the deacetylase domain from the PelDEFG inner membrane complex. Additionally, deacetylation is prioritized as it is required to export Pel through the electronegative exit channel formed by *Pa*PelC (18, 20, 21). Disruption of the interaction between *Pa*PelA and *Pa*PelB, release of PelA, or an alteration in how these proteins interact, could lead to less efficient deacetylation of the polymer and an increase in the percentage of GalNAc content in Pel. As the hydrolase domain of *Pa*PelA is more efficient at cleaving acetylated Pel (14, 19), PelA could then rapidly hydrolyze the polysaccharide (13). Determining how Pel binds to the deacetylase and hydrolase domain active sites of *Pa*PelA and the mechanisms of deacetylation and hydrolysis of the polysaccharide with respect to the *Pa*PelA–*Pa*PelB protein complex will be crucial for understanding how the Pel polysaccharide is modified for use in the biofilm matrix of *P. aeruginosa* and other Pel-producing bacteria.

Experimental procedures

Bacterial strains, plasmids, and growth conditions

A complete list of bacterial strains and plasmids used in this study can be found in Table S5. Terrific broth (TB) was used for the growth of the *E. coli* strains. TB contained, per liter of ultrapure water, 47.6 g of terrific broth and 0.4% (w/v) glycerol. No-salt lysogeny broth was used for the growth of the *P. aeruginosa* strains. No-salt lysogeny broth contained, per liter of ultrapure water, 10 g of tryptone and 5 g of yeast extract. Semisolid media was prepared by adding 1.5% (w/v) agar to LB. Where appropriate, kanamycin (Kan) at 50 μg/ml was added to growth media for *E. coli*.

Standard molecular methods

All basic microbiological and molecular biological techniques were performed using standard protocols. Genomic DNA was isolated using BioRad InstaGene Matrix. Plasmid isolation and DNA gel extraction was performed using purification kits purchased from BioBasic. Restriction enzymes, DNA ligase, alkaline phosphatase, and DNA polymerase were purchased from Thermo Fisher Scientific. Primers used in this study were obtained from Sigma-Aldrich (Table S6). Site-directed mutagenesis of plasmids was carried out using the Agilent QuikChange Lightning site-directed mutagenesis kit. Transformation of *E. coli* was performed using standard protocols. Sanger sequencing to confirm the sequence of plasmids and chromosomal mutations was performed at The Center for Applied Genomics, Toronto.

Cloning of recombinant proteins

The nucleotide sequence of *P. thermotolerans* H165_RS0111390 PelA (*Pt*PelA; accession WP_026146567) was obtained from The *Pseudomonas* DataBase and used to order a gene synthesis product cloned into the pET24a vector (BioBasic) (61). The PRED-TAT server indicated that *Pt*PelA is processed *via* the general secretion system (Sec) and has a signal sequence from residues 1 to 22. To obtain a soluble construct, the *Pt*PelA pET24a construct was used as a template to amplify the DNA of *Pt*PelA without the predicted signal sequence and at the start of the hydrolase domain (amino acids 37–937) (62). The restriction enzymes NcoI and XhoI were introduced and the gene was ligated into the pET28a expression vector encoding an N-terminal hexahistidine (His_6) tag. This generated the soluble *Pt*PelA construct used in the studies herein.

The site-directed mutants of *Pt*PelA and *Pa*PelA without its predicted signal sequence (amino acids 47–948 for *Pa*PelA; accession Q9HZE4) were generated using the QuikChange Lightning site-directed mutagenesis kit (Stratagene). The sequence of all vectors was confirmed using DNA sequencing.

Expression and purification

Expression and purification of WT *Pa*PelA (amino acids 47–948), the hydrolase construct of *Pa*PelA (amino acids 47–303), and *Pa*PelB (amino acids 47–880) has been described previously (18, 21, 43). Expression and purification of the double hydrolase mutant of *Pa*PelA was carried out as described for the WT protein. The expression of C-terminally His_6-tagged *Pt*PelA was achieved through the transformation of an expression vector into *E. coli* BL21 CodonPlus (DE3) cells, which was then grown in 1 L TB containing 50 μg/ml Kan at 37 °C. The cells were grown to an A_{600} of 0.8 to 1.0, at which point IPTG was added to a final concentration of 1 mM to induce expression. The induced cells were incubated for 20 h at 18 °C before being harvested *via* centrifugation at 6000*g* for 25 min at 4 °C. The pellet was stored at −20 °C until used.

The cell pellet was thawed and resuspended in 40 ml of wash buffer (20 mM Hepes pH 8, 300 mM NaCl, 10% (v/v) glycerol, 1 mM tris(2-carboxyethyl)phosphine, and 20 mM imidazole) containing one SIGMAFAST protease inhibitor ethylenediaminetetraacetic-free mixture tablet (Sigma). The resuspended cells were lysed with the sonicator 3000 (Misonix) for a processing time of 5 min. The pulse was applied on for 5 s and off for 10 s. The output level was 6.5. The insoluble lysate was removed by centrifugation at 25,000*g* for 30 min at 4 °C. The supernatant was loaded onto a 5 ml nickel-affinity column preequilibrated with 50 ml of wash buffer. The beads were then washed with 150 ml of wash buffer. Bound His_6-tagged protein was eluted using 50 ml of wash buffer containing 250 mM imidazole. Eluted protein was concentrated to 2 ml by centrifugation using Amicon Ultra centrifugal filters (Millipore) with a 50-kDa molecular weight cut-off (MWCO) at 3500*g* at a temperature of 4 °C. The protein was further purified using size-exclusion chromatography with a HiLoad 16/60 Superdex 200 gel filtration column (GE Healthcare) into a final buffer of 20 mM Hepes pH 8, 150 mM NaCl, 10 mM tris(2-carboxyethyl)phosphine, and 5% (v/v) glycerol. After gel filtration, protein fractions corresponding to greater than 95% purity on a 12% SDS-PAGE gel were pooled and concentrated using a 50-KDa MWCO Amicon Ultra centrifuge filter. Protein samples were divided into aliquots and

stored at −80 °C until use. The mutant constructs were expressed and purified as per the WT protein, and their folding and stability were assessed using differential scanning fluorimetry (Table S1).

Expression of the SeMet *Pt*PelA in a minimal medium was performed with a previously described protocol using B834 Met⁻ *E. coli* cells (Novagen) and subsequently purified using the protocol for the WT protein (63).

Crystallization, data collection, structure solution, and refinement

SeMet *Pt*PelA was screened for crystal hits using the sitting-drop vapor diffusion method with a Gryphon dropsetter (Art Robbins Instruments). Commercial sparse-matrix crystal screens MCSG1-4 (Microlytic) and JCSG TOP96 (Rigaku) were used to screen crystallization conditions. Trials were set up at room temperature and a protein concentration of 1.5, 3, or 5 mg/ml. In the Intelli 96-3 Shallow Well plates (Hampton), 2 μl drops at a 1:1 protein to mother liquor ratio were set up over a reservoir containing 100 μl of crystallization solution. Crystals were visible in many conditions after 5 days. Crystals that formed in 0.17 M ammonium sulfate, 0.085 M sodium citrate pH 5.6, 25.5% (w/v) PEG4000, and 15% (v/v) glycerol (TOP96 condition #A10) were harvested and vitrified in liquid nitrogen. Se-SAD data were collected at the National Synchrotron Light Source-II using the AMX beamline (17ID-1) at −173 °C (0.2° oscillations, 360°, 0.01 s/image) on two different regions of the same crystal, resulting in two datasets, DS#1 and DS#2. These datasets were processed using XDS (64) and merged with xprep (Bruker); Rmerge(DS#1) = 12.9%, Rmerge(DS#2) = 17.8%, and Rmerge(DS#1+#2) = 15.2%. The structure was solved using the SHELX suite (65). A total of twelve out of sixteen selenium sites in *Pt*PelA had significant anomalous signal and were located by SHELXD (65) using a resolution cut-off of 2.5 Å for the anomalous signal. SHELXE was initially able to build a poly-alanine trace for 381 residues, and the preliminary-phased electron density map was subsequently used for model building in COOT (66). Residues 750 to 791 were built manually into the density. Remaining residues were placed by superposing the AF2 model of PtPelA onto the built structure. The AF2 model was then divided into four fragments based on the domain architecture and rigid-body real-space refinements of these fragments against the electron density map performed. The rigid-body refinements corrected for minor differences between the electron density and the orientations of the domains in the AF2 model. The fit of the fragments to the electron density was carefully evaluated and we found that in general, the AF2 model matched well to the unbuilt regions of electron density. Residues from the AF2 model not supported by electron density were deleted. The structure was validated using an omit map created in the PHENIX.REFINE (67, 68). There was no interpretable density for the His_6 tag and for the following residues: 83 to 105, 198, 321 to 323, 389 to 395, 417 to 420, 448, 588 to 614, and 703 to 718. Iterative refinement of the model was performed in real space using Coot and PHENIX.REFINE (67, 68) against the 2.09 Å resolution dataset DS#1 (Table 1). A total of 428 water molecules were added manually during the later stages of the refinement.

Structural analysis tools

Individual protein and complex structural model predictions were generated using the AF2 and AF3 Protein Structure Database (https://alphafoldserver.com). For AF2, predictions were generated using ColabFoldv.1.5.2 with default parameters (*i.e.*, alphafold2_multimer_v3) and PDB templates. Five structures for each complex were predicted and used without relaxation in Amber. The predicted local difference test per residue plot of the five models generated indicates that most regions of *Pa*PelA and *Pa*PelB have been predicted with over 80% confidence, except for the predicted inner membrane helix and α-rich regions of *Pa*PelB (Figs. S1 and S8). For AF3, default parameters were used as customization, which is not possible during modeling. All structural figures were generated using PyMOL (The PyMOL Molecular Graphics System, Version 1.2, SchrÖdinger, LLC) and ChimeraX 1.7 (Resource for Biocomputing Visualization, and Informatics RBVI, UCSF) (69). The DALI server was used to compare the structures of full-length and the individual domains of *Pt*PelA with existing structures in the Protein Data Base (29). All structural biology applications used in this project were compiled and configured by SBGrid (70).

Multiple sequence analysis

The amino acid FASTA sequences of the analyzed CE enzymes (PelA, *P. aeruginosa* PAO1; PgdA, *S. pneumoniae* – accession Q8DP63; HP0310, *Helicobacter pylori* ATCC 700392/26695 – accession O25080; IcaB, *Staphylococcus epidermidis* 35984 – accession Q5HKP8; PgaB, *E. coli* K12 – accession P75906; and Agd3, *A. fumigatus* Af293 – accession Q4WX15) were retrieved from the *Pseudomonas* Genome DataBank (Pseudomonas.com) or UniProt (71). Multiple sequence alignment was performed using the Clustal Omega server (72).

AMMU esterase assay to detect metal dependency

This assay was performed as previously described (44). Thawed WT and mutant *Pt*PelA was diluted to 1 μM in the assay buffer (50 mM Hepes pH 7 and 75 mM NaCl) and kept on ice. The protein was then serially diluted from 1.11 μM to 1.1 nM. The AMMU substrate was dissolved in dimethyl sulfoxide prior to use at a concentration of 444 μM. In PCR strip tubes, 20 μl of protein was incubated with 2.5 μl of MilliQ water, 100 mM metal, or 25 mM metal chelator for 10 min. Reactions were initiated when 2.5 μl of AMMU was added to the enzyme reactions solutions to a total reaction volume of 25 μl. From the PCR strip tubes, 10 μl from the reaction solution were added to a 384-well black bottom plate (Corning 3820) in duplicate and centrifuged at 3000 RPM for 30 s. Reaction progress was monitored in real time by measuring the RFU at 30 s intervals over 10 min at room temperature. The λ_{emm} and λ_{ext} used were 330 and 450 nm, respectively.

The background hydrolysis was monitored and subtracted from the enzyme-catalyzed reactions. All assays were performed in quadruplicate using a BioTek Synergy Neo2 plate reader (Agilent Technologies). Prism (GraphPad Software Inc) was used for all analyses.

Microtiter dish biofilm disruption assays

This assay was performed as previously described (43). An overnight culture of PA14 was grown in LB-NS and normalized to an A_{600} of 0.5, then diluted to an A_{600} of 0.005 in 1 ml of LB-NS. Hundred microliters of normalized cells were added to the wells of 96-well anionic Corning CellBind plates and incubated statically for 24 h at 25 °C. Following incubation, nonattached cells were removed, and the plate was rinsed thoroughly three times with water. 142.5 μl of PBS solution was added to the wells. The protein was serially diluted from 60 to 0.06 μM in PBS, and 7.5 μl of each protein sample was added to the wells (n = 3 for each concentration). After incubating for 1 h at room temperature with shaking, the plate was rinsed thoroughly three times with water. The plates were then stained with 150 μl of 0.1% (w/v) crystal violet for 10 min at room temperature. The plate was rinsed, adhered crystal violet was solubilized in 150 μl of 100% (v/v) ethanol for 10 min at room temperature, and then the absorbance at 595 nm was measured to quantify adhered cells. Prism (GraphPad Software Inc) was used for all analyses.

Biochemical characterization of enzyme activity by MALDI-TOF MS

For all enzymes, a mix of α-(1,4)-GalNAc oligomers of various degrees of polymerization was used as substrate. Oligosaccharides were prepared as previously described (19). Briefly, 24 h-old biofilms of *A. fumigatus* Af293 were incubated with 10 nM Sph3 in 0.1× PBS for 1 h. Released oligosaccharides were then purified on C18 Sep-pak column.

The hydrolase activity of *Pt*PelA was observed after incubating the α-(1,4)-GalNAc oligosaccharides with 1 μM of enzyme in 1× PBS for 1 h at 37 °C. The hydrolase activity of *Pa*PelA was observed after incubating the α-(1,4)-GalNAc oligosaccharides with 1 μM of enzyme in 20 mM Hepes pH 8, 150 mM NaCl, and 5% (v/v) glycerol for 15 min, 1 h, and 3 h at room temperature in the absence or presence of 1.5 μM *Pa*PelB. The deacetylase activity of *Pa*PelA was observed after incubating the α-(1,4)-GalNAc oligosaccharides with 15 μM of *Pa*PelA double hydrolase mutant (E218A and D160A) in the same buffer used for WT enzyme for 24 h at 37 °C with or without 10 μM *Pa*PelB.

After each digestion, oligosaccharides were purified from the enzymes and salt on Hypersep HyperCarb Sep-pak columns and eluted with 100% CAN. Eluates were dried down under airflow and reconstituted in 10 μl of 0.2% TFA before being spotted onto a MALDI plate in 2,5-dihydroxybenzoic acid matrix as previously reported. Analysis of the oligosaccharide population by MALDI-TOF MS was acquired in positive reflectron mode, accumulating at least 10,000 shots on Bruker UltrafleXtreme equipment. Prism (GraphPad Software Inc) was used for the final analyses.

Homolog identification and analysis

*Pa*PelA^{AF2} was submitted to FoldSeek with an E-value cut-off of 0.03 and five iterations, resulting in the identification of 96 full-length sequences (73). The sequences were aligned by Clustal Omega in Geneious Prime 2023 (74). The alignment was then analyzed using FastTree v2 implemented within Geneious Prime 2023 using the *E. coli* lipoprotein LpoB (GenBank accession number WP_000164439.1) as an outgroup (75). The amino acid sequence of PelA from *P. aeruginosa* was also submitted to BLASTP with a cut-off value of 1e-03 with a sequence cap of 1000 (52). Only 177/1000 of the sequences identified in the BLASTP search were full-length and used in this study. When possible, BioCyc was used to identify Pel-like operons in the genomes of PelA homologs identified in the FoldSeek and BLASTP searches (76).

Data availabilty

The coordinates and structure factors for *Pt*PelA have been deposited in the Protein Data Bank, Accession number: 9CGY.

Supporting information—This article contains supporting information (18, 20, 21, 43, 44, 78).

Acknowledgments—We thank Greg Wasney from the SickKids Structural & Biophysical Core (SBC) facility for using the equipment and having constructive discussions.

Author contributions—J. C. V. L., F. L. M., R. P., Z. A. M., E. R., M. N., D. C. S., and P. L. H. writing–review and editing; J. C. V. L. and P. L. H. writing–original draft; J. C. V. L. and P. L. H. visualization; J. C. V. L., F. L. M., M. A. V., S. G., R. P., Z. A. M., and E. R. investigation; J. C. V. L. and P. L. H. formal analysis; J. C. V. L., M. A. V., and P. L. H. conceptualization; M. N., D. C. S., and P. L. H. supervision; M. N., D. C. S., and P. L. H. resources; M. N., D. C. S., and P. L. H. funding acquisition; P. L. H. project administration.

Funding and additional information—This work was supported in part by grants from the Canadian Institutes of Health Research (CIHR) to P. L. H. (MOP 43998 and FDN154327). P. L. H. was the recipient of a Tier 1 Canada Research Chair (2006-2020). This research has been supported by graduate student scholarships from the Province of Ontario (J. C. V. L.), The Hospital for Sick Children Foundation Student Scholarship Program (J. C. V. L.), and the Natural Science and Engineering Research Council of Canada (J. C. V. L.).

Conflict of interest—The authors declare that they have no conflicts of interest with the contents of this article.

Abbreviations—The abbreviations used are: AMMU, acetoxymethyl-4-methylumbelliferone; CE, carbohydrate esterase; GH, glycoside hydrolase; MALDI-TOF, matrix-assisted laser desorption/ionization-time of flight; MS, mass spectrometry; PNAG, poly-

β(1,6)-N-acetylglucosamine; SeMet, selenomethionyl-incorporated; TB, terrific broth; TPR, tetratricopeptide repeat.

References

1. Flemming, H.-C., and Wingender, J. (2010) The biofilm matrix. *Nat. Rev. Microbiol.* **8**, 623–633
2. Karygianni, L., Ren, Z., Koo, H., and Thurnheer, T. (2020) Biofilm matrixome: extracellular components in structured microbial communities. *Trends Microbiol.* **28**, 668–681
3. Pang, Z., Raudonis, R., Glick, B. R., Lin, T.-J., and Cheng, Z. (2019) Antibiotic resistance in Pseudomonas aeruginosa: mechanisms and alternative therapeutic strategies. *Biotechnol. Adv.* **37**, 177–192
4. Mulcahy, L. R., Isabella, V. M., and Lewis, K. (2014) Pseudomonas aeruginosa biofilms in disease. *Microb. Ecol.* **68**, 1–12
5. Salerian, A. J. (2020) Burn wound infections and Pseudomonas aeruginosa. *Burns* **46**, 257–258
6. Ghafoor, A., Hay, I. D., and Rehm, B. H. A. (2011) Role of exopolysaccharides in Pseudomonas aeruginosa biofilm formation and architecture. *Appl. Environ. Microb.* **77**, 5238–5246
7. Jennings, L. K., Storek, K. M., Ledvina, H. E., Coulon, C., Marmont, L. S., Sadovskaya, I., *et al.* (2015) Pel is a cationic exopolysaccharide that cross-links extracellular DNA in the Pseudomonas aeruginosa biofilm matrix. *Proc. Natl. Acad. Sci. U. S. A.* **112**, 11353–11358
8. Colvin, K. M., Gordon, V. D., Murakami, K., Borlee, B. R., Wozniak, D. J., Wong, G. C. L., *et al.* (2011) The pel polysaccharide can serve a structural and protective role in the biofilm matrix of Pseudomonas aeruginosa. *PLoS Pathog.* **7**, e1001264
9. Jennings, L. K., Dreifus, J. E., Reichhardt, C., Storek, K. M., Secor, P. R., Wozniak, D. J., *et al.* (2021) Pseudomonas aeruginosa aggregates in cystic fibrosis sputum produce exopolysaccharides that likely impede current therapies. *Cell Rep.* **34**, 108782
10. Khan, W., Bernier, S. P., Kuchma, S. L., Hammond, J. H., Hasan, F., and O'Toole, G. A. (2010) Aminoglycoside resistance of Pseudomonas aeruginosa biofilms modulated by extracellular polysaccharide. *Int. Microbiol.* **13**, 207–212
11. [preprint] Katharios, S. L., Whitfield, G. B., Howell, P. L., and O'Toole, G. A. (2020) Pseudomonas aeruginosa uses c-di-GMP phosphodiesterases RmcA and MorA to regulate biofilm maintenance. *bioRxiv*. https://doi.org/10.1101/2020.06.26.174680
12. Madsen, J. S., Lin, Y.-C., Squyres, G. R., Price-Whelan, A., Torio, A. de S., Song, A., *et al.* (2015) Facultative control of matrix production optimizes competitive fitness in Pseudomonas aeruginosa PA14 biofilm models. *Appl. Environ. Microbiol.* **81**, 8414–8426
13. Razvi, E., Whitfield, G. B., Reichhardt, C., Dreifus, J. E., Willis, A. R., Gluscencova, O. B., *et al.* (2023) Glycoside hydrolase processing of the Pel polysaccharide alters biofilm biomechanics and Pseudomonas aeruginosa virulence. *NPJ Biofilms Microbiomes* **9**, 7
14. Mauff, F. L., Razvi, E., Reichhardt, C., Sivarajah, P., Parsek, M. R., Howell, P. L., *et al.* (2022) The Pel polysaccharide is predominantly composed of a dimeric repeat of α-1,4 linked galactosamine and N-acetylgalactosamine. *Commun. Biol.* **5**, 502
15. Friedman, L., and Kolter, R. (2004) Genes involved in matrix formation in Pseudomonas aeruginosa PA14 biofilms. *Mol. Microbiol.* **51**, 675–690
16. Whitney, J. C., and Howell, P. L. (2013) Synthase-dependent exopolysaccharide secretion in Gram-negative bacteria. *Trends Microbiol.* **21**, 63–72
17. Whitfield, G. B., Marmont, L. S., Ostaszewski, A., Rich, J. D., Whitney, J. C., Parsek, M. R., *et al.* (2020) Pel polysaccharide biosynthesis requires an inner membrane complex comprised of PelD, PelE, PelF, and PelG. *J. Bacteriol.* **202**, e00684-19
18. Colvin, K. M., Alnabelseya, N., Baker, P., Whitney, J. C., Howell, P. L., and Parsek, M. R. (2013) PelA deacetylase activity is required for pel polysaccharide synthesis in Pseudomonas aeruginosa. *J. Bacteriol.* **195**, 2329–2339
19. Mauff, F. L., Bamford, N. C., Alnabelseya, N., Zhang, Y., Baker, P., Robinson, H., *et al.* (2019) Molecular mechanism of Aspergillus fumigatus biofilm disruption by fungal and bacterial glycoside hydrolases. *J. Biol. Chem.* **294**, 10760–10772
20. Marmont, L. S., Rich, J. D., Whitney, J. C., Whitfield, G. B., Almblad, H., Robinson, H., *et al.* (2017) Oligomeric lipoprotein PelC guides Pel polysaccharide export across the outer membrane of Pseudomonas aeruginosa. *Proc. Natl. Acad. Sci. U. S. A.* **114**, 2892–2897
21. Marmont, L. S., Whitfield, G. B., Rich, J. D., Yip, P., Giesbrecht, L. B., Stremick, C. A., *et al.* (2017) PelA and PelB proteins form a modification and secretion complex essential for Pel polysaccharide-dependent biofilm formation in Pseudomonas aeruginosa. *J. Biol. Chem.* **292**, 19411–19422
22. Little, D. J., Poloczek, J., Whitney, J. C., Robinson, H., Nitz, M., and Howell, P. L. (2012) The structure- and metal-dependent activity of Escherichia coli PgaB provides insight into the partial de-N-acetylation of poly-β-1,6-N-acetyl-d-glucosamine*. *J. Biol. Chem.* **287**, 31126–31137
23. Little, D. J., Pfoh, R., Mauff, F. L., Bamford, N. C., Notte, C., Baker, P., *et al.* (2018) PgaB orthologues contain a glycoside hydrolase domain that cleaves deacetylated poly-β(1,6)-N-acetylglucosamine and can disrupt bacterial biofilms. *PLoS Pathog.* **14**, e1006998
24. Keiski, C.-L., Harwich, M., Jain, S., Neculai, A. M., Yip, P., Robinson, H., *et al.* (2010) AlgK is a TPR-containing protein and the periplasmic component of a novel exopolysaccharide secretin. *Structure* **18**, 265–273
25. Gheorghita, A. A., Li, Y. E., Kitova, E. N., Bui, D. T., Pfoh, R., Low, K. E., *et al.* (2022) Structure of the AlgKX modification and secretion complex required for alginate production and biofilm attachment in Pseudomonas aeruginosa. *Nat. Commun.* **13**, 7631
26. Pfoh, R., Subramanian, A. S., Huang, J., Little, D. J., Forman, A., DiFrancesco, B. R., *et al.* (2022) The TPR domain of PgaA is a multifunctional scaffold that binds PNAG and modulates PgaB-dependent polymer processing. *PLoS Pathog.* **18**, e1010750
27. Pike, A. C. W., Garman, E. F., Krojer, T., von Delft, F., and Carpenter, E. P. (2016) An overview of heavy-atom derivatization of protein crystals. *Acta Crystallogr. Sect. D Struct. Biol.* **72**, 303–318
28. [preprint] Mirdita, M., Ovchinnikov, S., and Steinegger, M. (2021) ColabFold - making protein folding accessible to all. *bioRxiv*. https://doi.org/10.1101/2021.08.15.456425
29. Holm, L. (2020) DALI and the persistence of protein shape. *Protein Sci.* **29**, 128–140
30. Jensen, J. B., Peters, N. K., and Bhuvaneswari, T. V. (2002) Redundancy in periplasmic binding protein-dependent transport systems for trehalose, sucrose, and maltose in sinorhizobium meliloti. *J. Bacteriol.* **184**, 2978–2986
31. Li, Q.-A., Mavrodi, D. V., Thomashow, L. S., Roessle, M., and Blankenfeldt, W. (2011) Ligand binding induces an ammonia channel in 2-Amino-2-desoxyisochorismate (ADIC) synthase PhzE. *J. Biol. Chem.* **286**, 18213–18221
32. Taschner, M., Weber, K., Mourão, A., Vetter, M., Awasthi, M., Stiegler, M., *et al.* (2016) Intraflagellar transport proteins 172, 80, 57, 54, 38, and 20 form a stable tubulin-binding IFT-B2 complex. *EMBO J.* **35**, 773–790
33. Drula, E., Garron, M.-L., Dogan, S., Lombard, V., Henrissat, B., and Terrapon, N. (2021) The carbohydrate-active enzyme database: functions and literature. *Nucleic Acids Res.* **50**, D571–D577
34. Bamford, N. C., Mauff, F. L., Loon, J. C. V., Ostapska, H., Snarr, B. D., Zhang, Y., *et al.* (2020) Structural and biochemical characterization of the exopolysaccharide deacetylase Agd3 required for Aspergillus fumigatus biofilm formation. *Nat. Commun.* **11**, 2450
35. Blair, D. E., Schüttelkopf, A. W., MacRae, J. I., and van Aalten, D. M. F. (2005) Structure and metal-dependent mechanism of peptidoglycan deacetylase, a streptococcal virulence factor. *Proc. Natl. Acad. Sci. U. S. A.* **102**, 15429–15434
36. Little, D. J., Bamford, N. C., Pokrovskaya, V., Robinson, H., Nitz, M., and Howell, P. L. (2014) Structural basis for the de-N-acetylation of poly-β-1,6-N-acetyl-d-glucosamine in gram-positive bacteria. *J. Biol. Chem.* **289**, 35907–35917
37. Deng, D. M., Urch, J. E., ten Cate, J. M., Rao, V. A., van Aalten, D. M. F., and Crielaard, W. (2009) Streptococcus mutans SMU.623c codes for a functional, metal-dependent polysaccharide deacetylase that modulates interactions with salivary agglutinin. *J. Bacteriol.* **191**, 394–402

38. Zhang, Y., Wang, L., Overkleeft, H. S., van der Marel, G. A., and Codée, J. D. C. (2022) Assembly of a library of pel-oligosaccharides featuring α-glucosamine and α-galactosamine linkages. *Front. Chem.* **10**, 842238
39. Nakamichi, Y., Watanabe, M., Matsushika, A., and Inoue, H. (2020) Substrate recognition by a bifunctional GH30-7 xylanase B from Talaromyces cellulolyticus. *FEBS Open Bio* **10**, 1180–1189
40. John, F. J. S., González, J. M., and Pozharski, E. (2010) Consolidation of glycosyl hydrolase family 30: a dual domain 4/7 hydrolase family consisting of two structurally distinct groups. *FEBS Lett.* **584**, 4435–4441
41. Ji, S., Dix, S. R., Aziz, A. A., Sedelnikova, S. E., Baker, P. J., Rafferty, J. B., *et al.* (2019) The molecular basis of endolytic activity of a multidomain alginate lyase from Defluviitalea phaphyphila, a representative of a new lyase family, PL39. *J. Biol. Chem.* **294**, 18077–18091
42. Nishitani, Y., Horiuchi, A., Aslam, M., Kanai, T., Atomi, H., and Miki, K. (2018) Crystal structures of an archaeal chitinase ChiD and its ligand complexes. *Glycobiology* **28**, 418–426
43. Baker, P., Hill, P. J., Snarr, B. D., Alnabelseya, N., Pestrak, M. J., Lee, M. J., *et al.* (2016) Exopolysaccharide biosynthetic glycoside hydrolases can be utilized to disrupt and prevent Pseudomonas aeruginosa biofilms. *Sci. Adv.* **2**, e1501632
44. Razvi, E., DiFrancesco, B. R., Wasney, G. A., Morrison, Z. A., Tam, J., Auger, A., *et al.* (2023) Small molecule inhibition of an exopolysaccharide modification enzyme is a viable strategy to block Pseudomonas aeruginosa pel biofilm formation. *Microbiol. Spectr.* **3**, e00296-23
45. DiFrancesco, B. R., Morrison, Z. A., and Nitz, M. (2018) Monosaccharide inhibitors targeting carbohydrate esterase family 4 de-N-acetylases. *Bioorgan Med. Chem.* **26**, 5631–5643
46. Lambert, C., Lerner, T. R., Bui, N. K., Somers, H., Aizawa, S.-I., Liddell, S., *et al.* (2016) Interrupting peptidoglycan deacetylation during Bdellovibrio predator-prey interaction prevents ultimate destruction of prey wall, liberating bacterial-ghosts. *Sci. Rep.* **6**, 26010
47. Liu, L., Zhou, Y., Qu, M., Qiu, Y., Guo, X., Zhang, Y., *et al.* (2019) Structural and biochemical insights into the catalytic mechanisms of two insect chitin deacetylases of the carbohydrate esterase 4 family. *J. Biol. Chem.* **294**, 5774–5783
48. Andrés, E., Albesa-Jové, D., Biarnés, X., Moerschbacher, B. M., Guerin, M. E., and Planas, A. (2014) Structural basis of chitin oligosaccharide deacetylation. *Angew. Chem. Int. Ed.* **53**, 6882–6887
49. Andreou, A., Giastas, P., Arnaouteli, S., Tzanodaskalaki, M., Tzartos, S. J., Bethanis, K., *et al.* (2019) The putative polysaccharide deacetylase Ba0331: cloning, expression, crystallization and structure determination. *Acta Crystallogr. F. Struct. Biol. Commun.* **75**, 312–320
50. Abramson, J., Adler, J., Dunger, J., Evans, R., Green, T., Pritzel, A., *et al.* (2024) Accurate structure prediction ofbiomolecular interactions with AlphaFold 3. *Nature* **630**, 493–500
51. van Kempen, M., Kim, S. S., Tumescheit, C., Mirdita, M., Lee, J., Gilchrist, C. L. M., *et al.* (2023) Fast and accurate protein structure search with Foldseek. *Nat. Biotechnol.* https://doi.org/10.1038/s41587-023-01773-0
52. Sayers, E. W., Bolton, E. E., Brister, J. R., Canese, K., Chan, J., Comeau, D. C., *et al.* (2021) Database resources of the national center for biotechnology information. *Nucleic Acids Res.* **50**, D20–D26
53. Bundalovic-Torma, C., Whitfield, G. B., Marmont, L. S., Howell, P. L., and Parkinson, J. (2020) A systematic pipeline for classifying bacterial operons reveals the evolutionary landscape of biofilm machineries. *PLoS Comput. Biol.* **16**, e1007721
54. Cerveny, L., Straskova, A., Dankova, V., Hartlova, A., Ceckova, M., Staud, F., *et al.* (2013) Tetratricopeptide repeat motifs in the world of bacterial pathogens: role in virulence mechanisms. *Infect. Immun.* **81**, 629–635
55. [preprint] Benedens, M., Hernandez, C. R., Straathof, S. A. P., Loschwitz, J., Berninghausen, O., Maglia, G., *et al.* (2024) Assembly and dynamics of the outer membrane exopolysaccharide transporter PelBC of Pseudomonas aeruginosa. *bioRxiv*. https://doi.org/10.1101/2024.09.23.614597
56. Taylor, E. J., Gloster, T. M., Turkenburg, J. P., Vincent, F., Brzozowski, A. M., Dupont, C., *et al.* (2006) Structure and activity of two metal ion-dependent acetylxylan esterases involved in plant cell wall degradation reveals a close similarity to peptidoglycan deacetylases*. *J. Biol. Chem.* **281**, 10968–10975
57. Strunk, R. J., Piemonte, K. M., Petersen, N. M., Koutsioulis, D., Bouriotis, V., Perry, K., *et al.* (2014) Structure determination of BA0150, a putative polysaccharide deacetylase from Bacillus anthracis. *Acta Crystallogr. Sect. F: Struct. Biol. Commun.* **70**, 156–159
58. Manaia, C. M. (2002) Pseudomonas thermotolerans sp. nov., a thermotolerant species of the genus Pseudomonas sensu stricto. *Int. J. Syst. Evol. Microbiol.* **52**, 2203–2209
59. Crone, S., Vives-Flórez, M., Kvich, L., Saunders, A. M., Malone, M., Nicolaisen, M. H., *et al.* (2020) The environmental occurrence of Pseudomonas aeruginosa. *APMIS* **128**, 220–231
60. Shaik, M. M., Cendron, L., Percudani, R., and Zanotti, G. (2011) The structure of Helicobacter pylori HP0310 reveals an atypical peptidoglycan deacetylase. *PLoS One* **6**, e19207
61. Winsor, G. L., Griffiths, E. J., Lo, R., Dhillon, B. K., Shay, J. A., and Brinkman, F. S. L. (2016) Enhanced annotations and features for comparing thousands of Pseudomonas genomes in the Pseudomonas genome database. *Nucleic Acids Res.* **44**, D646–D653
62. Bagos, P. G., Nikolaou, E. P., Liakopoulos, T. D., and Tsirigos, K. D. (2010) Combined prediction of Tat and Sec signal peptides with hidden Markov models. *Bioinformatics* **26**, 2811–2817
63. Lee, J. E., Cornell, K. A., Riscoe, M. K., and Howell, P. L. (2001) Structure of E. coli 5′-methylthioadenosine/S-adenosylhomocysteine nucleosidase reveals similarity to the purine nucleoside phosphorylases. *Structure* **9**, 941–953
64. Kabsch, W. (2010) Integration, scaling, space-group assignment and post-refinement. *Acta Crystallogr. Sect. D Biol. Crystallogr.* **66**, 133–144
65. Usón, I., and Sheldrick, G. M. (2018) An introduction to experimental phasing of macromolecules illustrated by SHELX; new autotracing features. *Acta Crystallogr. D. Struct. Biol.* **74**, 106–116
66. Emsley, P., Lohkamp, B., Scott, W. G., and Cowtan, K. (2010) Features and development of Coot. *Acta Crystallogr. Sect. D Biol. Crystallogr.* **66**, 486–501
67. Liebschner, D., Afonine, P. V., Baker, M. L., Bunkóczi, G., Chen, V. B., Croll, T. I., *et al.* (2019) Macromolecular structure determination using X-rays, neutrons and electrons: recent developments in Phenix. *Acta Crystallogr. D. Struct. Biol.* **75**, 861–877
68. Chen, V. B., Arendall, W. B., Headd, J. J., Keedy, D. A., Immormino, R. M., Kapral, G. J., *et al.* (2010) MolProbity: all-atom structure validation for macromolecular crystallography. *Acta Crystallogr. Sect. D Biol. Crystallogr.* **66**, 12–21
69. Pettersen, E. F., Goddard, T. D., Huang, C. C., Meng, E. C., Couch, G. S., Croll, T. I., *et al.* (2021) UCSF ChimeraX: structure visualization for researchers, educators, and developers. *Protein Sci.* **30**, 70–82
70. Morin, A., Eisenbraun, B., Key, J., Sanschagrin, P. C., Timony, M. A., Ottaviano, M., *et al.* (2013) Collaboration gets the most out of software. *eLife* **2**, e01456
71. Consortium, T. U., Bateman, A., Martin, M.-J., Orchard, S., Magrane, M., Agivetova, R., *et al.* (2020) UniProt: the universal protein knowledgebase in 2021. *Nucleic Acids Res.* **49**, D480–D489
72. Sievers, F., and Higgins, D. G. (2018) Clustal Omega for making accurate alignments of many protein sequences. *Protein Sci.* **27**, 135–145
73. Potter, S. C., Luciani, A., Eddy, S. R., Park, Y., Lopez, R., and Finn, R. D. (2018) HMMER web server: 2018 update. *Nucleic Acids Res.* **46**, W200–W204
74. Sievers, F., Wilm, A., Dineen, D., Gibson, T. J., Karplus, K., Li, W., *et al.* (2011) Fast, scalable generation of high-quality protein multiple sequence alignments using Clustal Omega. *Mol. Syst. Biol.* **7**, 539
75. Price, M. N., Dehal, P. S., and Arkin, A. P. (2010) FastTree 2 – approximately maximum-likelihood trees for large alignments. *PLoS One* **5**, e9490
76. Karp, P. D., Billington, R., Caspi, R., Fulcher, C. A., Latendresse, M., Kothari, A., *et al.* (2017) The BioCyc collection of microbial genomes and metabolic pathways. *Brief. Bioinform.* **20**, 1085–1093
77. Ren, J., Wen, L., Gao, X., Jin, C., Xue, Y., and Yao, X. (2009) Dog 1.0: illustrator of protein domain structures. *Cell Res.* **19**, 271–273
78. Lee, M. J., Geller, A. M., Bamford, N. C., Liu, H., Gravelat, F. N., Snarr, B. D., *et al.* (2016) Deacetylation of fungal exopolysaccharide mediates adhesion and biofilm formation. *Mbio* **7**, e00252–16